Soft Matter

REVIEW

View Article Online
View Journal | View Issue

Cite this: *Soft Matter*, 2024, **20**, 3554

Theory and simulation of ligand functionalized nanoparticles – a pedagogical overview

Thi Vo

Synthesizing reconfigurable nanoscale synthons with predictive control over shape, size, and interparticle interactions is a holy grail of bottom-up self-assembly. Grand challenges in their rational design, however, lie in both the large space of experimental synthetic parameters and proper understanding of the molecular mechanisms governing their formation. As such, computational and theoretical tools for predicting and modeling building block interactions have grown to become integral in modern day self-assembly research. In this review, we provide an in-depth discussion of the current state-of-the-art strategies available for modeling ligand functionalized nanoparticles. We focus on the critical role of how ligand interactions and surface distributions impact the emergent, pre-programmed behaviors between neighboring particles. To help build insights into the underlying physics, we first define an "ideal" limit – the short ligand, "hard" sphere approximation – and discuss all experimental handles through the lens of perturbations about this reference point. Finally, we identify theories that are capable of bridging interparticle interactions to nanoscale self-assembly and conclude by discussing exciting new directions for this field.

Received 5th February 2024,
Accepted 11th April 2024

DOI: 10.1039/d4sm00177j

rsc.li/soft-matter-journal

Introduction

Materials complexity required to make modern day technologies and devices has grown exponentially, especially in recent years.[1–13] For example, wearable electronics necessitate multifunctional soft materials that combine high flexibility, high power density, and efficient energy generation into a small, portable device.[14–16] Similarly, membrane and separation technologies require materials with molecular scale resolution in selectivity to be fabricated with low to zero defects at the micron/millimeter length scales.[17–24] Lastly, soft robotics require materials that are mechanically stable yet highly malleable so that they can be reconfigured under load/stimuli.[25–28] While there are many additional examples related to photonic,[29,30] sensing,[2,3,31] and catalytic[32,33] properties, the feature pervading across every single case is that the core design aspects involve combining multiple components into a single, composite entity. There are barriers, however, that arise from such a requirement. Achieving the level of precision spatial ordering needed to obtain the desired macroscopic properties is often undermined by kinetic traps, as multicomponent systems are more susceptible to fabrication defects. Furthermore, depending on the chemical species, phase segregation can counteract co-assembly to disrupt the emergence of desired properties.

Efforts to bypass these constraints have progressively shifted towards self-assembly as an alternative route to top-down approaches for materials fabrication.[34–43] Such an approach is of interest due to the ability to pre-program interactions into each individual building block unit, enabling nanoscale control over interparticle spatial/orientation ordering beyond what is achievable *via* top-down methods. Over the past several decades, research on self-assembly has resulted in a suite of nanoscale building blocks capable of achieving long-range structural ordering at the mesoscale.[40,44,45] This toolkit spans

Chemical and Biomolecular Engineering, Johns Hopkins University, Baltimore, MD 21218, USA. E-mail: tvo12@jhu.edu

Thi Vo

Thi Vo is an Assistant Professor of Chemical and Biomolecular Engineering at Johns Hopkins University. He received his BS at Rice University and PhD at Columbia University. He was a postdoctoral researcher at the University of Michigan and has been at Hopkins since 2022. Vo is a theoretician who specializes in polymer and nanoscale self-assembly. His research aims at developing insights into fundamental interactions to design complex building blocks for materials fabrication. Vo can be reached by email at tvo12@jhu.edu.

a diverse range of techniques that include surface modifications,[46–50] emulsion-templating,[51] solvent evaporation,[52,53] and microphase separation.[54,55] Amongst this expansive library, shape anisotropy and nanoparticle (NP) ligand functionalization have emerged as two popular strategies that are now widely used for controlling assembly.[40,56] For clarity, shape anisotropy is defined as the usage of NPs whose shapes are aspherical, that is, cubic, octahedral, tetrahedral, *etc*. With respect to ligands, our definition encompasses a wide range of different chemical species that include short oligomers (*i.e.* oleic acids, alkanes, and dendrimers), polymers, and DNA oligonucleotides. These two design handles readily synergize with each other to produce a distinct class of building blocks called ligand functionalized nanoparticles (LNPs). To date, there have been excellent reviews that cover both synthesis and experimentally observed assemblies of LNPs.[40,44,45,57,58] As such, we refer the reader to those works for current experimental advances.

Our focus in this review is to provide a comprehensive overview of state-of-the-art computational and theoretical modeling approaches developed for predicting LNP self-assembly to complement the experimental literature. We specifically focus on linking ligand conformations and ligand surface distributions about the NP core to emergent LNP interactions to highlight the physical driving forces governing LNP self-assembly. These insights are correlated to key features needed for the construction of interaction potentials to accurately translate experimental parameters to coarse-grained computational models. Due to the expansive nature of LNPs, we organize our review into two broad categories of ligand types employed in NP functionalization – short *versus* long ligands. For long ligands, we additionally split discussion into three ligand classes: (1) oligomeric, (2) polymeric, and (3) DNA-based. For each of the four ligand types, we discuss their functionalization onto spherical and polyhedral NPs to dissect the interplay between geometry and ligand features in directing LNP interactions and self-assembly (Fig. 1).

While such classifications are based on ligand chemistry and/or NP core geometry to provide concrete connections to experimentally synthesizable systems, the selected demarcations

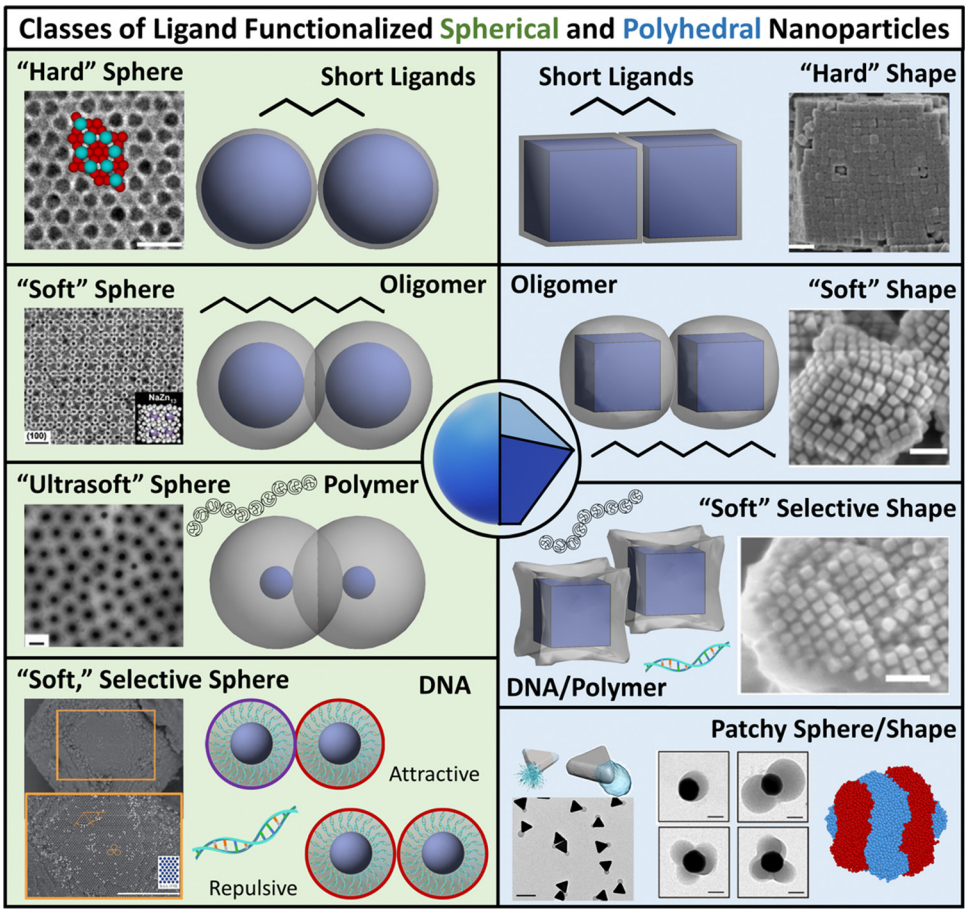

Fig. 1 Classes of ligand functionalized nanoparticles. We organize LNPs into subcategories to facilitate discussion of theory/simulations. Specifically, we define 4 classes of ligands (short, oligomeric, polymeric, and DNA) and 2 classes of NP cores (spherical and polyhedral), totaling 8 different types of LNPs. Corresponding emergent inter-LNP interaction types (hard, soft, directional, *etc*.) are also indicated for each classification. The figure contains images reproduced from ref. 42, 43, 48, 72, 79, 109, 142, 182–184; ref. 42, 43, 72, 183 and 48 with permission from Springer Nature (© 2006, 2011, 2020, 2021, and 2022); ref. 182, 109 and 184 with permission from the American Chemical Society (© 2013 and 2021); ref. 79 with permission from the American Association for the Advancement of Science (© 2019); and ref. 142 with permission from Wiley (© 2023).

directly correlate to the emergent nature of the inter-LNP attraction/repulsion. For example, short ligands give rise to hard particle interactions while oligomers/polymers manifest into softer, deformable, and more complex interaction potentials. In this way, our classifications provide a direct connection between molecular features associated with ligand chemistry and particle geometry and a unique type of inter-LNP interaction. In other words, each defined LNP category can be mapped to a class of effective interactional potentials, providing a roadmap for computational modeling of experimental systems. For all ligand/geometry based classifications discussed, we explicitly highlight the corresponding class of coarse-grained interaction potentials within their respective sections.

To build intuition and physical understanding for each class of LNP, we specifically explain the underlying physics of how the interplay between core–core, ligand–core, and ligand–ligand interactions sculpts the shape of the ligand shell (corona) and how corona morphology can be used to predict LNP interactions. We then provide context on how the predicted interaction potentials are employed in simulations of LNP self-assembly. In particular, we discuss guiding heuristics that can be utilized to approximate potential parameters based on experimental handles. Key takeaways are highlighted at the end of each section to emphasize how each perturbation in design parameters (ligand length, core geometry, ligand architecture, solvent conditions, *etc.*) influences emergent inter-LNP interactions and hierarchical self-assembly. For our discussions, we first establish the ''hydrogen atom'' equivalent for LNPs – spherically symmetric particles whose interactions are dominated by steric repulsion (*i.e.* the hard sphere model). We then iteratively increase LNP complexity as a function of both ligand chemistry and core geometry. Each additional complexity is contrasted against those previously discussed to help establish intuition as to how each additional aspect builds upon each other to sculpt the emergent inter-LNP interactions. As a final note, we discuss theoretical capabilities for *a priori* prediction of LNP self-assembly for each class of LNPs and conclude by presenting new directions where advances in theory and computational modeling of LNPs are needed to guide experiments.

Short ligand functionalization

We start at one simplifying extreme of LNP designs: high NP surface coverage (grafting density, σ) using short, sterically repulsive ligands. In this limit, traditional approaches assume that ligands are isotropically distributed on the NP surface and the corona shape of the ligand coating is conformal to the underlying NP shape. Our discussion here is split into two subcategories: spherical NP cores and polyhedral NP cores.

Spherical NPs with short ligands – hard sphere interaction

For spherical NP cores, the LNP behaves effectively as a larger sphere whose hydrodynamic radius is the NP core radius plus the thickness of the ligand shell. More quantitatively, the boundary for grafting density and ligand lengths is as follows: firstly, ligand grafting density must be at or near the limit of full coverage ($\sigma \geq 1.0$ nm^{-2}). Secondly, the ligand length N must be on the order of $N \leq R_{\text{core}}\sigma^{1/2}$, where R_{core} is the NP radius.[59] This crossover is obtained by determining the radial distance from the surface at which the monomer density is no longer unitary ($r_s \sim R_{\text{core}}\sigma^{1/2}b$). Due to the high monomer density, the monomers must be organized in a radially linear manner. This means that r_s must also scale as $r_s \sim Nb$. Substituting for r^* immediately yields the crossover condition in N. Another way to interpret the length constraint is by requiring that $R_g \ll R_{\text{core}}$, where R_g is the ligand's radius of gyration and R_{core} is the NP radius. The physical manifestation of these boundaries in N and σ is that ligand conformations within the corona behave akin to rigid rods anchored at one end to the NP surface. Coupled with the sterically repulsive nature of the functionalized ligands, this means that inter-LNP interactions are completely driven by steric repulsion. The only constraint for LNPs in this limit is that they cannot occupy the same space as other LNPs as there is an infinitely strong repulsive force preventing such overlaps. All other forces that govern how particles should interact with their neighbors are negligible in this limit. For this reason, common approaches employed to model interactions between LNPs with short ligands are the hard sphere (HS) and the Weeks–Chandler–Anderson (WCA) potentials[60] (Fig. 2a).

The HS potential takes the following form:[61]

$$V(r) = \begin{cases} \infty & r \leq a \\ 0 & r > a \end{cases} \quad (1)$$

where a is the particle diameter. This potential captures the idea that LNPs have a dense ligand shell that cannot deform nor interpenetrate with one another: that is, the NP core + ligand shell behaves like a perfectly hard composite particle whose hydrodynamic radius a is equal to the core radius plus the shell thickness. Here, to connect the HS diameter a to experimental handles N and σ, we note that the thickness of a fully stretched, ligand brush in good solvent scales[62] as $N\sigma^{1/3}b$. In essence, the ligand is so short that the spherical NP core appears planar relative to the ligand size. As such, we expect a qualitative scaling of $a \sim N\sigma^{1/3}b$ to map experimental parameters to the coarse-grained HS size in eqn (1). Usage of the HS potential in Monte Carlo simulations dates back to the earliest days in computer experiments of particle self-assembly and crystallization.[61,63–66] Despite its simplicity, the HS model can accurately capture both single-component and multi-component systems of spherical LNP crystallizations. Perhaps one of its biggest successes is the ability to capture the expansion in assembly diversity in transitioning from unary to binary (or higher) systems. In the limit of single-component, the HS model readily captures known experimental formation of face-centered cubic or body-centered cubic lattices.[67] In transitioning to multi-component systems, generalizations of eqn (1) to incorporate spheres of different sizes in simulation can reproduce the observed formation of Laves phases[68] (Fig. 2b), 2D

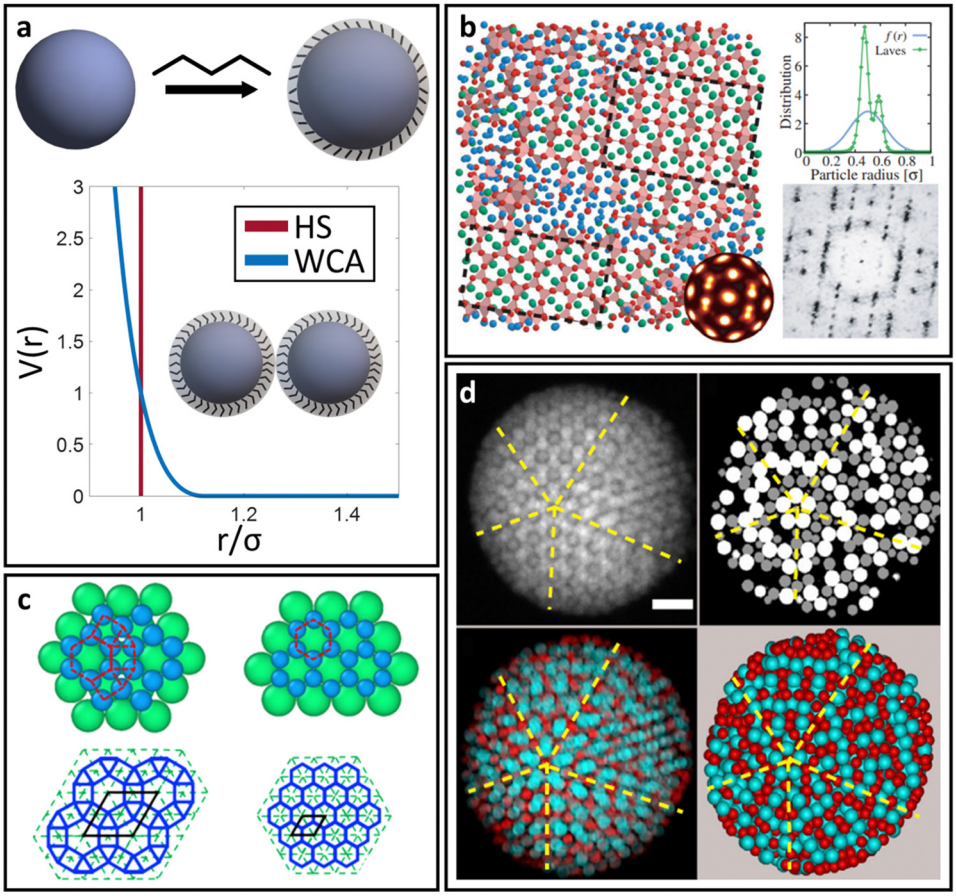

Fig. 2 "Hard" spherical LNPs. (a) Emergent interaction between "hard" spherical LNPs: HS or WCA interaction. Binary hard sphere assembly into (b) Laves phases,[68] (c) periodically tessellating and honeycomb 2D lattices,[69] and (d) spherically confined icosahedral clusters.[72] Figures are reproduced from ref. 68 with permission from the American Physical Society (© 2019) and ref. 72 and 69 with permission from Springer Nature (© 2020 and 2022).

periodic architectures[69] (Fig. 2c), Frank–Kasper phases,[68] quasicrystals,[70] chiral spherical helices under confinement,[71] and even magic number icosahedral clusters[72,73] (Fig. 2d).

A corollary to eqn (1) is the WCA potential:[60]

$$V(r) = \begin{cases} 4\varepsilon\left[\left(\frac{a}{r}\right)^{12} - \left(\frac{a}{r}\right)^{6}\right] + \varepsilon, & r \le 2^{1/6}a \\ 0 & r > 2^{1/6}a \end{cases} \quad (2)$$

The HS potential (eqn (1)) is only applicable for Monte Carlo (MC) simulations as it is discontinuous and therefore is not energy conserving. To define a conservative inter-LNP potential for molecular dynamics (MD) simulations, the WCA potential was developed (eqn (2)). By construction, this potential is purely repulsive up to the interparticle distance of $2^{1/6}a$, beyond which there are no interacting forces between neighboring LNPs. Here, qualitative mapping of ε to experimental handles should scale with $\sigma^{1/2}$. This behavior arises from inter-ligand distance D scaling[62] as $\sigma^{-1/2}$. Decreasing D correlates to decreasing space between neighboring ligands, increasing the "hardness" of the HS-like LNP. Similar to the HS potential, connecting a to experimental handles involves correlating the particle size to the ligand brush thickness of $N\sigma^{1/3}b$. Applications of the WCA potential for MD simulations have reproduced known behaviors observed in MC simulations.[74] More importantly, they also enable the study of LNP dynamics for systems where the HS assumptions are valid. Examples include measurement of thermodynamics properties such as specific heat and elasticity coefficients,[75] diffusivity/hopping mechanisms,[76,77] and assembly pathways of LNP crystallization.[78]

Key takeaway. Functionalizing short, sterically repulsive ligands at high coverage onto spherical NPs creates a densely packed ligand shell where steric hinderances dominate to produce an emergent hard sphere effect. As a result, inter-LNP interactions for functionalized NPs in this region of ligand parameter space are theoretically and computationally modeled using hard-sphere or sterically repulsive (WCA) potentials. The prolific success in capturing such diverse morphologies indicates that the hard-sphere approximation accurately captures the underlying physics for self-assembly of LNPs functionalized with short ligands. Due to the simplicity of the emergent interactions, we define this as the ideal limit for LNPs. All other LNPs are discussed through the lens of perturbations about this ideal limit to build insight into the underlying physics of ligand functionalization.

Polyhedral NPs with short ligands – hard shape interaction

A common perturbation about the ideal LNP limit is the usage of polyhedral, as opposed to spherical, NPs. In this section, we again consider the case of high grafting density and short, sterically repulsive ligands. This ensures that NP geometry is the sole difference relative to the ideal HS limit discussed above. Similar to spherical geometry, strong steric repulsion between functionalized ligands results in high ligand extension and a uniform ligand distribution about the NP surface (isotropic grafting). As such, the corona shape is conformal to the underlying geometry of the polyhedral NP core and the LNP can be modelled as a hard polyhedron whose size is the core size plus the thickness of the ligand shell (Fig. 3d). With respect to grafting density, the quantitative boundary is analogous to that of spherical NPs: ($\sigma \geq 1.0\ \mathrm{nm}^{-2}$). However, the same is not true for the ligand length. Unlike spheres, polyhedral NPs possess surface locations of varying curvatures. High curvature surfaces impose less spatial confinement due to an increase in local free volume available per unit of solid angle. This means that a ligand of identical length can relax away from its rigid, rod-like configuration when anchored to high curvature locations thanks to decreased confinement. As such, the upper limit for ligand length must incorporate the effect of local curvature. Accounting for the relevant geometrical packing constraints, the curvature corrected upper limit for ligand length to enforce the "hard" polyhedron limit is: $N \sim R_{\mathrm{core}}\sigma^{1/2}\Omega^{-3/2}$, where R_{core} here defines the polyhedral NP's insphere radius and Ω defines the distance from the NP surface to its center of mass, normalized by its insphere radius.[79] As a clarifying example, in the case of a cubic NP, $\Omega = 1, \sqrt{2},$ and $\sqrt{3}$ for the face, edge, and corner, respectively. In the limit of a spherical NP core, Ω = 1 and this constraint converges back to the HS limit for ligand length. Note that the curvature effect is inversely related to the maximum ligand length. This reflects the physical picture discussed above where a shorter ligand is necessary at high curvatures to maintain both a high density within the ligand shell and enforce zero ligand interpenetration between LNPs. Within this regime, theoretical modeling of inter-LNP interactions in the dilute limit is a simple extension of the HS (eqn (1)) and WCA (eqn (2)) to account for shape anisotropy.

Analytical generalizations of the HS potential to polyhedral geometry do not exist. However, adapting shape overlap detection protocols such as the Gilbert–Johnson–Keerthi algorithm[80] (GJK) or Minkowski Portal Refinement[81] (MPR) from the computer graphics literature provides a way to obtain an algorithmic

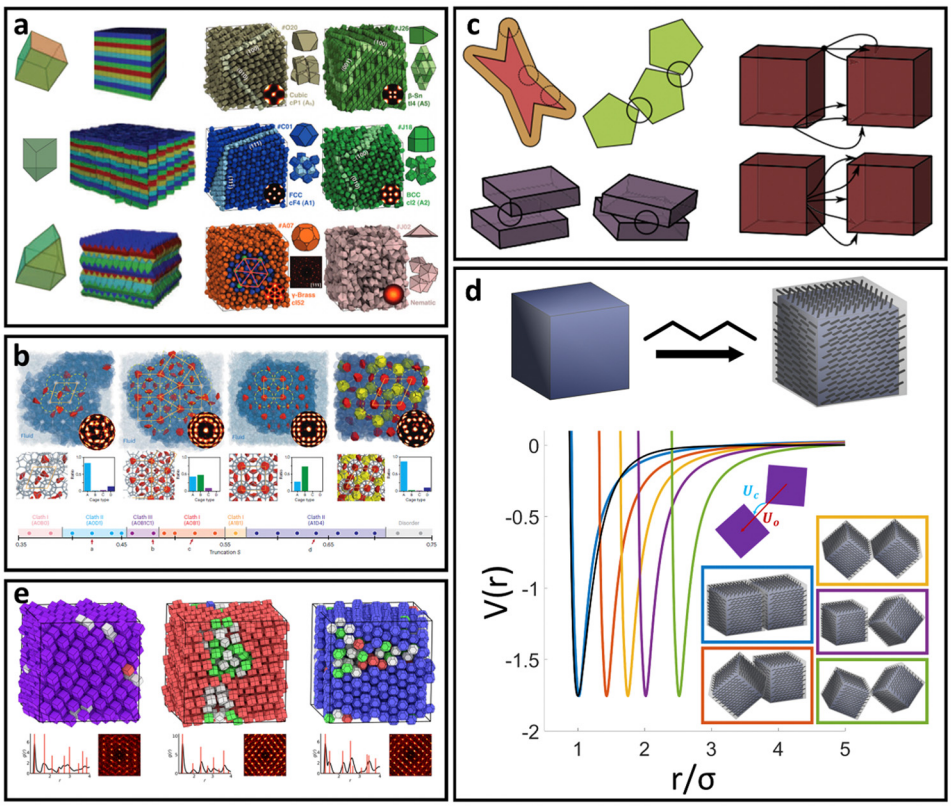

Fig. 3 "Hard" polyhedral LNPs. MC self-assembly of hard polyhedra yields a diverse suite of (a) closed-packed, high entropy structures[82,83] and (b) host–guest, open lattice structures.[90] MD simulation of hard polyhedra is enabled either by (c) DEM[96] or (d) a generalized anisotropic version of common isotropic potentials (here WCA).[98] (e) MD simulation using the anisotropic WCA potential reproduces known results from MC.[98] Figures are reproduced from ref. 82 and 90 with permission from Springer Nature (© 2011 and 2023); ref. 83 with permission from the American Association for the Advancement of Science (© 2012); ref. 96 with permission from Elsevier (© 2017); and ref. 98 with permission from the American Institute of Physics (© 2020).

formulation of the HS potential (eqn (1)) for all convex polyhedral shapes. Briefly, both algorithms define support mappings that reduce overlap detection between complex shapes to a series of Minkowski difference calculations between triangles (2D) or tetrahedra (3D). This complexity reduction allows on-the-fly shape overlap checks, making GJK and MPR ideal for simulation based overlap calculations. Similar to the HS model, polyhedral dimensions in MC are proportional to the thickness of the ligand layer. Utilizing a qualitative dependence of $a \sim N\sigma^{1/3}b$ enables a mapping of experimental handles to the coarse-grained particle size. Coupling eqn (1) with shape overlap detection has enabled a diverse range of different MC simulations of hard polyhedral particles[82–84] (Fig. 3a). Seminal MC simulations for unary systems of hard polyhedral models for LNPs have reproduced the observed crystallization behaviors for a wide range of different core geometries.[43,85–87] Examples include the formation of simple cubic superlattices using cubic NPs,[82–84] Minkowski superlattices using octahedral NPs,[82–84] dodecagonal quasicrystalline morphologies using tetrahedral NPs,[88,89] and clathrate structures using pentagonal bipyramidal NPs[90,91] (Fig. 3b). Recent studies have also explored the space of multicomponent systems for hard polyhedra as well, yielding previously unobserved structures such as space-tiling assemblies of complementary polyhedra[92] and compartmentalization of non-complementary polyhedra into host–guest superlattices.[90] Due to the simplicity of the hard sphere approximation, MC simulations of experimentally unexplored hard polyhedral LNPs have also revealed a diverse suite of crystalline morphologies. These superlattices include open host–guest motifs,[90,93] complex layered crystals with 2, 3, or 4 unique Wyckoff sites, and even a Bergman-like superlattice with a 432-particle unit cell.[94]

To enable MD simulation of ''hard'' polyhedral LNPs, there are several approaches to capture anisotropic geometries within a pair potential. Here, our focus is on MD potentials that explicitly consider core geometry in their force evaluations. For the alternative case of creating an effective polyhedron *via* a superposition of WCA spheres, we refer the reader to the rigid body literature.[95] One approach takes advantages of discrete element methods (DEMs) commonly employed in finite element modeling (Fig. 3c). DEMs assign a WCA potential to all pairwise combinations of face, edge, and corner contacts between neighboring particles.[96] Doing so preserves all relevant facet interactions. A net force on the particle's center of mass is then computed by summing over all contributing WCA potentials between pairs of faces, corners, and edges. Using this approach, DEMs can reproduce assembly behaviors of simple shapes in MD. However, due to rounding artifacts arising from usage of a WCA potential at edge and corner facets, DEMs struggle to capture more complex superlattices like quasicrystal formation using tetrahedral LNPs or orientationally ordered face-centered cubic formation of rhombic dodecahedral LNPs. Efforts to address this ''rounding'' effect have led to the development of another class of anisotropic HS-like potentials based on computing effective potentials of mean force between shaped particles.[97,98] These approaches typically assume a set of particle configurations, which enable symmetry-dependent simplification of the multidimensional integrals used to compute the average force. The caveat, however, is that they are no longer amenable to ''on-the-fly'' force evaluations needed for MD simulation. One exception is a generalized mean-field approach that was developed to provide analytical functional forms for anisotropic variants of isotropic pair potentials[98] (Fig. 3d). In the limit of the WCA potential, the corresponding anisotropic WCA potential applies a contact potential between the closest surface points on two neighboring particles as shown below (eqn (3)):

$$V(r) = \begin{cases} 4\varepsilon_s\left[\left(\frac{a}{r}\right)^{12} - \left(\frac{a}{r}\right)^{6}\right] + 4\varepsilon\left[\left(\frac{a_c}{r_c}\right)^{12} - \left(\frac{a_c}{r_c}\right)^{6}\right] + \varepsilon_s + \varepsilon, & r \le 2^{1/6}a,\ r_c \le 2^{1/6}a_c \\ 0 & r > 2^{1/6}a,\ r_c > 2^{1/6}a_c \end{cases} \quad (3)$$

where a_c is the diameter of the sphere associated with the contact potential, r_c is the distance between the two closest surface points, and ε_s is a configuration dependent scaled interaction potential to ensure a conformal energy contour about the core geometry. This potential utilizes the GJK[80] algorithm to compute r_c for a given pairwise particle configuration and benefits from quick force evaluation thanks to its analytical form (eqn (3)). More importantly, it only requires the usage of a single WCA term for the closest point of contact between the shaped particles. This results in reduced rounding of particle geometry, enabling computational reproduction of complex ''hard'' polyhedral LNP assemblies observed in experiments and MC simulations (Fig. 3e). Conceptually, eqn (3) works by morphing a spherical core into its respective shape ''on-the-fly'' during force and torque calculations *via* the contact potential for every pairwise particle interaction (Fig. 3d). In all the above cases, mapping experimental parameters like ligand length (N) and grafting density (σ) involves the scaling relationship $a \sim N\sigma^{1/3}b$, similar to their MC counterparts. Analogous to the WCA potential (eqn (2)), a qualitative mapping of $\varepsilon \sim \sigma^{1/2}$ captures the increased steric repulsion between LNPs with increasing grafting densities. All other parameters (ε_s and a_c) in eqn (3) are uniquely defined given ε and a.

Key takeaway. ''Hard'' polyhedral LNPs deviate away from the ideal LNP limit along the experimental axis of NP shape. Here, the emergent shape of the corona is conformal to that of the core's geometry. This shift in inter-LNP interactions from hard sphere to that of hard polyhedra highlights the idea that particle overlap still dominates the energetics in the short ligand limit. While no analytical HS potential for polyhedral geometry exists, major advances in computational modeling and simulations have enabled rapid and systematic exploration of the particle geometry phase space to guide experimental synthesis.

Limitations of the "hard" LNP approximation

There are two caveats, however, that need to be considered for "hard" LNPs. While the above discussion applies to 3D polyhedral/spherical cores, care must be taken in the limit of 2D polygonal nanoplates or nanodiscs. This is because the plate/disc thickness (l_t) can often be small enough that $R_g \ll l_t$ no longer holds.[99] In fact, $R_g \sim l_t$ for most 2D cases. This indicates that the ligand size is on par with particle thickness. In this regime, entropy plays a major role in driving ligand partition and the ligand corona morphology is no longer conformal to the core geometry. We provide detailed discussion of such phenomena in the ligand functionalized polyhedral NPs section, where this effect dominates. Another important feature to consider is emergent directional interaction due to crowding (high LNP density). Hard polyhedra are known to exhibit preferential orientational orderings along their large facets that arise due to entropy maximization.[100–102] This means that inter-LNP interactions no longer follow the HS limit and emergent directional forces start to play a larger role. Care, therefore, must be taken when trying to model "hard" polyhedral LNPs outside of the dilute concentration regime. We provide a discussion of this effect in the "Theoretical prediction of LNP self-assembly" section.

Long ligand functionalization on spherical NPs

In this category, we relax the constraint of short ligands for spherical LNPs but keep the high grafting density limit. There are now 3 classes of ligands that are of specific interest: (1) oligomers with the degree of polymerization $N > R_{core}\sigma^{1/2}$, (2) polymeric chains, and (3) DNA oligonucleotides. Furthermore, DNA oligonucleotides and polymeric ligands have an additional handle of tunable attraction/repulsion between different ligand species enabled by complementary base-pairing and molecular recognition terminal units,[103] respectively. This feature makes DNA/polymeric ligands popular for binary LNP systems as they enable species-specific control over inter-LNP interactions. We consider all the above in our discussion of long ligand functionalization of spherical NPs.

Regardless of oligomeric, DNA, or polymeric ligand type, the major change relative to the "hard" spherical LNP limit lies in how ligands are organized within the corona as they are no longer forced to take on a rigid, rod-like morphology due to strong confinement. This transition arises purely from geometry and consideration of the local free volumes available between neighboring functionalized ligands. For a spherical geometry, the volume of a spherical sector (V_{ss}) grows with increasing radial distance r_s away from the NP surface for any given solid angle Γ: that is, $V_{ss} = 3^{-1}\Gamma r_s{}^3$. As a result, monomers located near the non-functionalized terminal of the ligand (*i.e.* those sitting further away from the NP surface) have more space available to them relative to monomers near the ligand's anchored head. The net result is a decrease in local confinement experienced by all monomers located at distances $r_s > R_{core}\sigma^{1/2}b$, which ultimately enhances ligand flexibility.[79] This additional flexibility makes the "hard" LNP approximation invalid for ligand parameters within this regime.

Spherical NPs with oligomeric ligands – soft sphere interaction

For oligomeric ligands, ligand–ligand interactions and corona morphologies are still dominated by steric interactions. However, unlike the hard sphere limit where high confinement creates an impenetrable ligand shell, the increased flexibility associated with longer ligands results in a splaying of their linear conformation when in close contact with a neighboring oligomer functionalized LNP. Depending on the local coordination of particles surrounding a reference LNP, different degrees of splaying can occur.[104] The net effect is an increase in local free volume available to each ligand that favors interpenetration between neighboring coronas. This is because ligand intercalation is energetically favored compared to conformational entropy loss and increased bond tension associated with ligand compression. In other words, LNPs are no longer impenetrable and we obtain an effectively "soft" sphere whose corona can deform as needed to minimize its total free energy (Fig. 4a). When considering oligomeric ligands, the extent of ligand splaying, emergent corona shape, and degree of corona overlap can all be predicted using the Orbifold Topological Model.[104–106]

The net effect of this complex interplay between ligand splaying, local free volume, and corona interpenetration is the emergence of an attractive potential well between LNPs.[105,107–110] It is here that the starkest contrast between "hard" and "soft" LNPs becomes apparent. Unlike the hard sphere limit, there is an optimal center-to-center separation that arises from the presence of an attractive well between two LNPs. For this reason, the Mie potential is commonly used to model the class of oligomeric LNP interactions[111] (Fig. 4a):

$$V(r) = \frac{n}{n-m}\left(\frac{n}{m}\right)^{\frac{m}{n-m}}\varepsilon\left[\left(\frac{a}{r}\right)^{n} - \left(\frac{a}{r}\right)^{m}\right] \quad (4)$$

with the constraint of $m < n$. By inspection, the Mie potential (eqn (4)) is a generalization of the WCA potential (eqn (2)) for different exponents, with an analogous cutoff of $r < \left(\frac{n}{m}\right)^{\frac{1}{n-m}}a$. In the limit of $n = 12$ and $m = 6$, both equations are identical. In short, the Mie potential is a more versatile variant of the WCA potential and can be employed to capture both attractive and repulsive interactions between LNPs. Transitioning from eqn (2) to (4) now yields four parameters (a, ε, n and m) that must be mapped correctly to meaningful trends from experimental systems. In general, there are two common approaches. The first involves measuring the second virial coefficient (B_2) between LNPs in experiments and then fitting to analytical expression from statistical mechanics: $B_2 = -2\pi\int\left[e^{-\beta V(r)} - 1\right]r^2\,dr$. This approach has recently been employed to model experimentally measured LNP emergent interaction.[112] While B_2 fitting can yield constants for eqn (4) that accurately captures experimentally observed LNP interactions, measurements of B_2 are often not readily available.

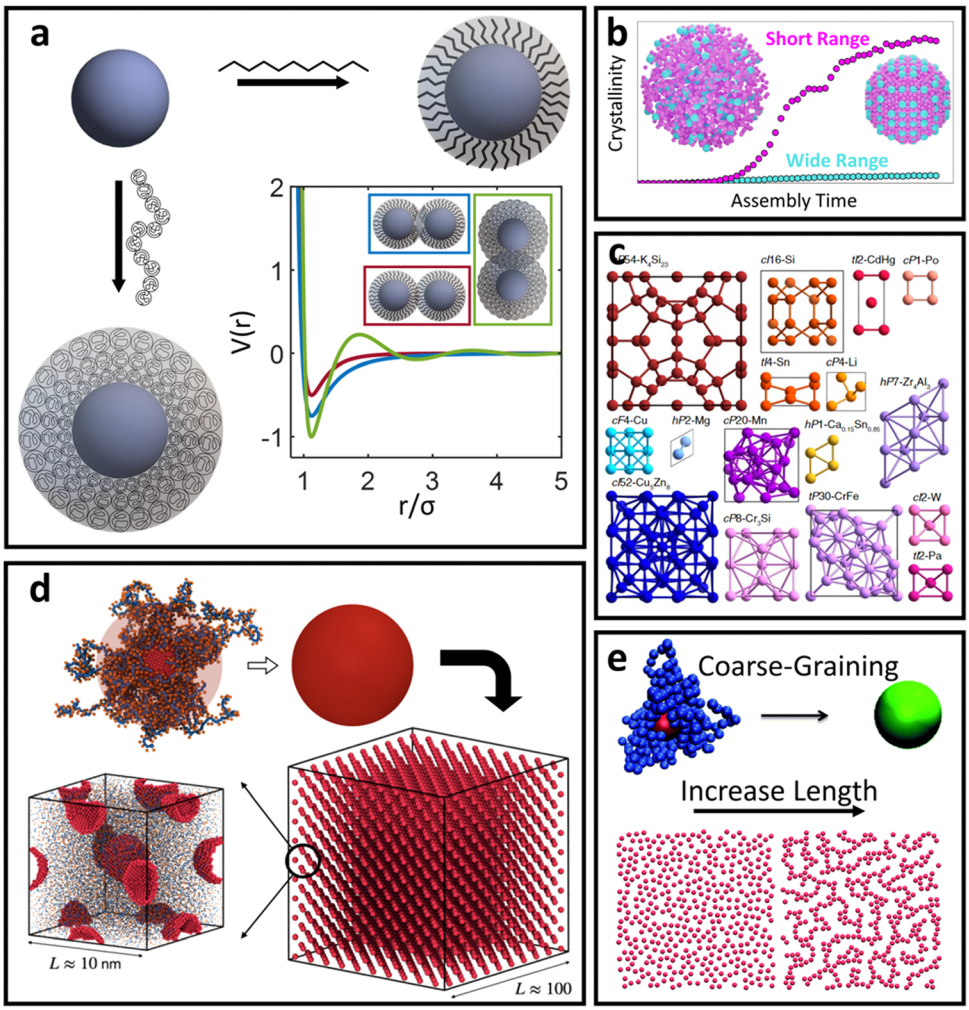

Fig. 4 "Soft" spherical LNPs – oligomeric/polymeric ligands. (a) Emergent interaction between oligomer/polymer functionalized spherical NPs. Soft, compressible ligands can produce a net attraction with a variable range or even multi-well interaction potentials. (b) Net short range attraction can speed up assembly dynamics.[112] (c) Multi-well interactions can produce a diverse suite of self-assembled lattices.[116] Coarse-grained interaction potential can also reduce complexity to capture assembly of (d) 3D superlattices of polymer functionalized NPs[125] or (e) 2D LNP networks.[124] Figures are reproduced from ref. 112 with permission from Springer Nature (© 2023); ref. 116 with permission from the National Academy of Sciences (© 2021); and ref. 124 and 125 with permission from the Royal Society of Chemistry (© 2014 and 2023).

The alternative approach is similar to the mappings discussed in the short ligand limit, where one can utilize scaling behaviors to qualitatively correlate experimental handles to potential parameters. Due to the increase in the ligand length, the ligand thickness now has the form $N^{1/2}\sigma^{1/4}b$. This means that mapping experimental parameters to the particle size a in eqn (4) scales with $N^{1/2}\sigma^{1/4}b$. Unlike with hard sphere and hard polyhedra, however, there are now three different parameters that all contribute to the interaction between LNPs: n, m, and ε. Tuning the relative difference between n and m alters the width of the attractive well associated with eqn (4) and provides a handle to tune corona overlaps between LNPs. Since inter-graft separation D scales as $\sigma^{-1/2}$, we expect that $\sigma^{1/2}$ captures the reduction in space available for corona interpenetration between neighboring LNPs. A counteracting effect, however, lies with increasing ligand lengths. Increasing N enhances ligand flexibility, which favors LNP interpenetration. Here, monomer density for oligomeric graft lengths typically scales[113] as $N^{-1/2}$. Therefore, we expect a composite mapping of n–m scaling as $N^{-1/2}\sigma^{1/2}$. Along the same vein, n also scales with $N^{-1/2}\sigma^{1/2}$ to capture reduction in corona interpenetration (*i.e.* increased hardness) of each LNP. Lastly, the slight corona overlap produces an emergent attraction between neighboring LNPs. By inspection, ε controls the well-depth and slope of eqn (4). We expect this to increase with the number of interacting monomers within the overlap region, thus yielding a mapping of $\varepsilon \sim N^{1/2}\sigma^{1/2}$. Usage of the Mie potential in MC and MD simulation of oligomer functionalized LNPs can capture the assembly behavior for a diverse range of single-component and multi-component "soft" LNPs made using oligomeric ligand functionalization. Examples include binary superlattices that are isostructural to intermellatic and/or ionic atomic lattices[114,115] or metallic coordination lattices[116] (Fig. 4c). Simulations also enabled studies that elucidate assembly features

such as stoichiometry-driven enhancement of crystallization rates[112] (Fig. 4b), superlattice spacing,[106] and the effect of confinement on self-assembly[112]

Key takeaway. Here, perturbation away from the ideal LNP limits lies in extending the ligand length to oligomers while keeping the same spherical core geometry. Increasing ligand length adds a degree of softness to LNPs, allowing the coronas to partially overlap with each other. In essence, the emergent effective interaction between oligomeric ligand functionalized NPs is congruent to that of ''soft'' spheres. However, constraints such as the impenetrable NP core and energetic costs of ligand deformation set an upper limit on the degree of LNP corona interpenetration.

Spherical NPs with polymeric ligands – ultra-soft sphere interaction

Deviations from the oligomeric limit start to occur when the size of the functionalized ligand is of a similar order of magnitude as the NP core size: $R_g \sim R_{core}$. Since R_{core} is on the nanometer scale, the R_g of a ligand at the transition point is at least an order of magnitude larger than those of traditional oligomeric ligands. By definition, ligands with sizes this large are typically considered to be polymers. Therefore, $R_g \sim R_{core}$ marks the transition from an oligomeric to a polymeric ligand. The key differences in corona behaviors within this limit can be better understood through analysis of the volumetric space available to functionalized ligands. Consider the spherical sector volume $V_{ss} \sim 3^{-1}\Gamma r_s^3$ (from before). A 10× increase in radial distance r_s would correspond to a 1000× increase in the volume available to a ligand given the same solid angle. In other words, monomers occupying the regions far away from the NP surface experience drastically lower confinement from neighboring ligands thanks to the increase in space availability. Polymer segments in these regions are free to explore their configurational space and take on more expanded conformations to maximize ligand entropy. There exists a large repository of theoretical works developed over the past several decades that can predict corona morphology arising from such expanded configurations for polymeric ligands functionalized onto flat,[117,118] curved,[119] dense cores (*i.e.* star polymers[113]), or NP surfaces.[120,121] Such theories can *a priori* predict how polymers are organized in concentric radial layers moving outward from the NP surface. The thickness of each layer is determined by balancing energetic contributions from thermal noise, monomer–monomer, monomer–solvent, and exclude volume interactions between neighboring polymeric ligands. The key predictions with respect to corona morphologies in these models are: (1) corona morphologies are spherical, reflecting the underlying NP shape and (2) low monomer density in regions far away from the NP surface. This means that corona interpenetration is highly favorable between neighboring LNPs as steric hinderance/repulsion between interacting polymeric ligands are at a minimum. Due to the high degree of corona overlap between LNPs, NPs functionalized with long polymeric ligands are typically considered to exhibit ''ultrasoft'' LNP interactions (Fig. 4a). As a result, the physical picture for interacting spherical NPs functionalized with polymeric ligands is that of highly overlapping spherical particles.

For polymeric ligands, there exist a diverse library of different effective interaction potentials that can be used to for either MC or MD simulations.[122–125] The functional forms of these potentials are either theoretically predicted from analytical theory,[122,126–128] adaptation of Mie and/or power law potentials,[129] or computationally measured using detailed, atomistic simulations.[107,121,124,125,130–132] Analytical potentials rely on geometrical arguments and integration over an averaged monomer density profile along the entire length of the functionalized polymer. Results from this approach often produce a logarithmic like behavior in center-to-center distance between particles: $V(r) \sim -\ln(a/r)$. These potentials typically exhibit both an attractive well and a soft repulsive shoulder to capture both short range attraction and longer range steric hinderances associated with fluctuating polymeric ligands (Fig. 4d and e). Due to the polymeric nature of the corona layer, mapping ligand parameters to particle size a utilized size of the grafted brush, which scales as $N^{3/5}\sigma^{1/5}b$ for a good solvent. It is assumed that good solvent scaling is typical for LNP self-assembly where particles need to be dispersed in solution to avoid aggregation and/or phase separation. Alternative approaches involve adapting the Mie potential by combining it with either long range repulsive potentials (Yukawa,[133] eqn (5)) or multi-barrier potentials (oscillating pair potential)[116] (eqn (6) or Dzugotov[134]) to mimic the theoretically predicted multi-well effective inter-LNP interactions. Examples of the functional form for each are shown below:

$$V(r) = \varepsilon\frac{e^{-\kappa r}}{r} \tag{5}$$

$$V(r) = \varepsilon_1 r_1^{(-n_1)} + \varepsilon_2 r_2^{(-n_2)}\cos(kr - \phi) \tag{6}$$

where κ is the distance scaling parameter, ε defines the interaction strength of each term, n_1 and n_2 are the exponents of the inverse r behaviors akin to the Mie exponents, and k and ϕ define the frequency and phase shift of the multiple potential barriers, respectively. The additional benefit of such a combinatorial approach is that computationally measured inter-LNP potentials tend to also exhibit singlet or multi-well potential behaviors. As such, eqn (4)–(6) provide an ideal basis set for parameter coarse-graining and fitting of measured interactions from detailed simulation data. Due to the fitting nature of eqn (4)–(6), mapping between all potential parameters to experimental handles becomes less clear. However, some broad trends can still be defined. Firstly, κ, k, and ϕ all define the attenuation distance of long-/short-range repulsion, which should correlate to the effective size of the LNP corona. Therefore, we anticipate an analogous mapping to a, which has the form $N^{3/5}\sigma^{1/5}b$. Secondly, mapping $n{-}m$ follows the same logic as in the oligomeric limit, but using good solvent scaling exponents: that is, $n{-}m \sim N^{-4/5}\sigma^{2/3}$. Similarly, we expect n_1 and n_2 from eqn (6) to also be influenced by corona interpenetration, yielding a mapping of $N^{-4/5}\sigma^{2/2}$. Thirdly, all ε parameters are related to attraction depths/slopes for their

respective potentials. Therefore, we anticipate analogous mapping to the oligomeric limit of $\varepsilon \sim N^{4/5}\sigma^{2/3}$ where again the different exponents reflect good solvent conditions. Lastly, recent experimental success in functionalizing hydrogen bonding or conjugated monomers to the free ends of polymeric ligands has enabled additional control over species specific interactions.[103] This means that an individual LNP can be preprogrammed to exhibit selective repulsive or attractive interactions with other LNPs. Since eqn (4)–(6) already include attractive and repulsive terms in their functional forms, they are immediately generalizable to such multicomponent systems. Relative ratios between values of ε for attraction/repulsion should reflect the ratio of a favorable number of monomer–monomer contacts between the interacting LNPs. Altogether, the results from eqn (4)–(6) provide a powerful suite of simple, coarse-grained potentials that can capture complex ''ultrasoft'' attractive and repulsive interactions between LNPs and polymeric ligands.

Key takeaway. Similar to oligomeric ligands, deviations away from the ideal LNP reference revolve around increasing ligand length to the polymeric limit. Here, the physical picture takes advantage of the idea that a polymer sweeps out a large volume of space due to its high number of chain conformations. Through the lens of a functionalized polymer, this means that regions far away from the NP surface only exhibit low monomer density and high polymer flexibility, resulting in energetically favorable overlap between neighboring coronas. The key takeaway for polymeric ligands is that the emergent inter-LNP interactions are analogous to ''ultrasoft'' spheres.

Spherical NPs with DNA ligands – soft, selective sphere interaction

In between the oligomeric and polymeric limits is the special case of DNA (*i.e.* oligonucleotides) ligands. There are two types of DNA that are commonly used for NP functionalization: single-stranded (ssDNA) and double-stranded (dsDNA). We first discuss the physical picture underlying inter-LNP interactions for both DNA ligand types and then present computational potentials commonly employed for simulating their assembly behaviors.

dsDNA ligands are stiff with long persistence length (rod-like behavior) due to the double-helix nature of the hybridized backbone.[135] This rod-like nature of dsDNA makes the ligand highly inflexible, prohibiting splaying and/or compression. Furthermore, the negatively charged backbone of the dsDNA ligands creates strong electrostatic repulsions that prevent interpenetration of the ligand shells.[136] Through this lens, spherical NPs with dsDNA ligands behave analogous to the hard-sphere limit, where interactions are dominated by steric repulsion between spheres with radii equal to the hydrodynamic radius of the functionalized NP core. The key difference, however, is that dsDNA ligands have unhybridized ''sticky-ends'' that imbue LNPs with additional attractive/repulsive interactions beyond steric effects. These ''sticky-ends'' are all positioned at the outermost edge of the ligand corona due to a combination of electrostatic backbone repulsion and rigid nature of the dsDNA double-helix.[136] As such, the net LNP interactions for dsDNA functionalized spherical NPs are that of selectively ''sticky'' hard spheres. More specifically, these LNPs exhibit hard sphere repulsion and uniformly distributed surface-localized attraction between NPs functionalized with non-complementary and complementary dsDNA, respectively (Fig. 5a).

In contrast, ssDNA ligands are more flexible due to the unhybridized nature of the functionalized DNAs. This means that effects related to ligand flexibility and confinement discussed earlier for oligomeric/polymeric ligands also apply to ssDNA. However, ssDNA still possesses a negatively charged backbone. The presence of electrostatic repulsion between neighboring ligands drives ligand extension and prevents excessive interpenetration between ligand shells, albeit not to the same extent as dsDNA. Altogether, this produces two regions of ssDNA organization in the LNP corona: interior and exterior. The interior region sits closer to the NP surface, where electrostatics and ligand extension dominate. The hard-sphere approximation directly applies in this interior regime. The exterior region possesses increased local free volume available to each ligand due to the r^3 dependence in V_{ss}, thereby reducing ligand–ligand electrostatic repulsion and providing space for ligand shell interpenetration. This means that ''sticky-ends'' are no longer forced to localize at the outer edge of the LNP corona but can exist anywhere inside the exterior region. The boundary between these two regimes sits at a distance $r_B = R_{core}\sigma^{1/2}\nu^{-1}b$ away from the NP surface, where ν is the excluded volume of a ssDNA Kuhn monomer.[79] Note that the boundary is of a similar order of magnitude to R_{core} and thus reflects the long ligand requirement for these effects to manifest in the DNA corona. For ssDNA lengths much less than R_{core}, the behavior is analogous to dsDNA.

Based on the physical picture discussed, a simple potential that captures inter-LNP interactions for both ssDNA and dsDNA ligands is the square well (SW) potential:[137]

$$V(r) = \begin{cases} \infty & r < a \\ -\varepsilon & a \le r < \lambda a \\ 0 & r \ge \lambda a \end{cases} \quad (7)$$

By inspection, the SW potential is an extension of the HS potential (eqn (1)), where an attractive region of width λ and well-depth ε has been added to the surface of a sphere with radius a. For cases where λ is small ($\lambda \ll a$), the SW potential exactly captures the attractive ''sticky-ends'' at the corona edge of dsDNA functionalized NPs. Larger values of λ allow a higher degree of overlap, shifting the SW potential to the ssDNA limit. For non-complementary ssDNA or dsDNA, $\varepsilon = 0$ and the SW potential converges to the HS limit to reflect the steric repulsion between LNP coronas. This feature reflects the idea that electrostatics dominate between noncomplementary DNA ligands, which results in hard sphere behaviors for LNPs. To map experimental handles to potential parameters in eqn (7), we first note that interactions between DNA are driven by base

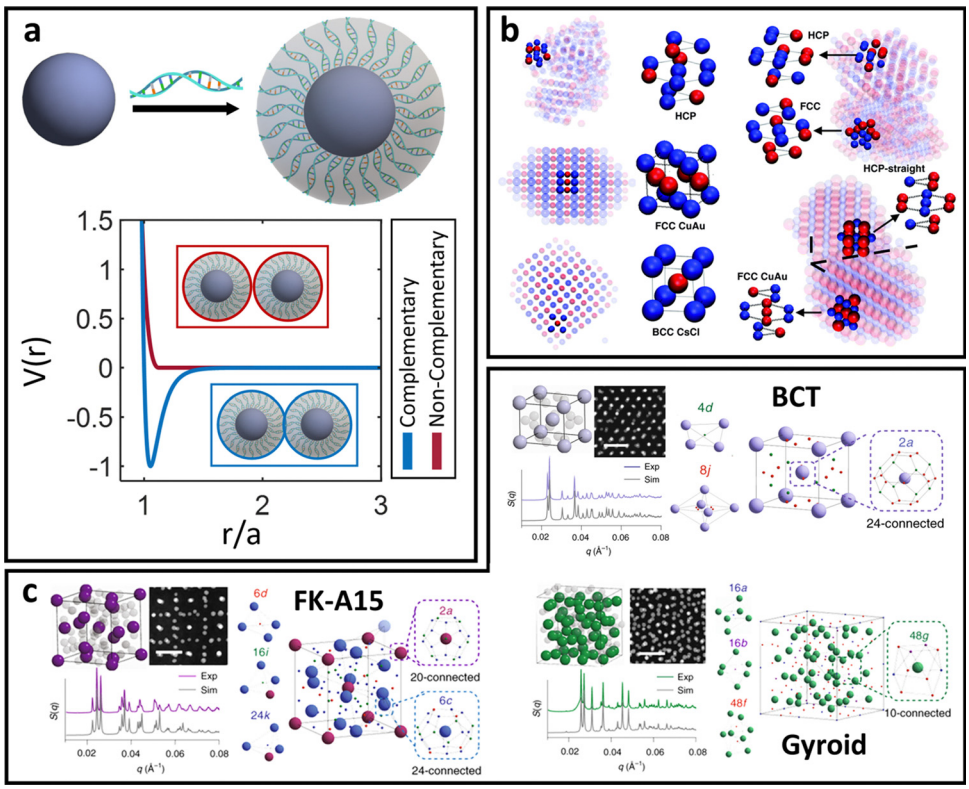

Fig. 5 "Soft" spherical LNPs – DNA ligands. (a) Emergent interaction between DNA functionalized spherical NPs. Complementary nature of DNA hybridization can give rise to both attraction and repulsions between particles. (b) Usage of "soft," partially overlapping potentials in MD can capture assembly of (b) common structures such as HCP, FCC, CuAu, and BCC lattices.[138] (c) Soft interaction potentials between DNA functionalized NPs can even drive the formation of low density morphologies such as the FK-A15 and Gyroid lattices.[141] Figures are reproduced from ref. 138 with permission from the Royal Society of Chemistry (© 2018) and ref. 141 with permission from Springer Nature (© 2022).

pairing. As such, the well depth ε should scale linearly with both the number of DNA sticky ends and grafting density: $\varepsilon \sim N_s\sigma$, where N_s is the number of "sticky-ends" on the DNA ligand. For dsDNA, the behavior of the DNA ligand is analogous to that of a rigid-rod, and we expect the same mapping of a to scale as $N\sigma^{1/3}$. For ssDNA, ligands are more flexible and behave akin to long ligands. Therefore, we anticipate a qualitative mapping of a to be $N^{3/5}\sigma^{1/5}b$. The interpenetration ratio λ for dsDNA typically scales with the ratio of the full stretch to the equilibrium length of the dsDNA "sticky-ends," yielding $\lambda \sim 1.25N_s$. For ssDNA, this interpenetration scales with the ratio of its hybridized to unhybridized lengths, which takes the form $\lambda \sim N^{2/5}$.

Similar to the HS potential, the SW potential is discontinuous and thus cannot be employed in MD simulations. In the limit of MD, the Mie (eqn (4)) or the Fermi–Jagla (FJ)[138] (eqn (8)) potentials are common alternatives to the SW potential. Mie potential features are already discussed above. We note that for dsDNA ligands, n and m are roughly on the order of $n = 50$ and $m = 25$ to enforce short-ranged interactions. Conversely, values of n and m are closer to those of the WCA potential (eqn (2)) for ssDNA to allow a longer interaction range and a higher degree of overlap between LNPs. In the ssDNA limit, we expect analogous mapping of experimental handles to potential parameters as those discussed for the Mie potential (eqn (4)). For the FJ potential, its functional form combines the power-law behavior in r with two additional terms designed to capture the interactions specific to DNA:

$$V(r) = \varepsilon\left[\left(\frac{a}{r}\right)^n + \frac{A_0}{1+e^{\left[\frac{A_1}{A_0}\left(\frac{r}{a}-A_2\right)\right]}} - \frac{B_0}{1+e^{\left[\frac{B_1}{B_0}\left(\frac{r}{a}-B_2\right)\right]}}\right] \quad (8)$$

where $A_0, A_1, A_2, \ldots, B_2$ are parameters that tune the range and strength of repulsive/attractive interactions. Terms with constants A_i account for steric repulsion between dsDNA ligands and terms with constants B_i build in LNP attraction arising from "sticky-end" hybridization. Since both sets of A_i and B_i terms scale with respect to the number of "sticky-ends," we anticipate qualitative mappings for both to scale with $N_s\sigma$ (analogous to the SW potential mapping). Mapping of the particle size is also analogous to the SW potential for each respective DNA ligand type. Common self-assembled superlattices traditionally observed for DNA ligands on spherical NPs have been observed in using the above simulation models. In the single-component limit with self-complementary DNA ligands, simple lattices such as NaCl, face-centered cubic, and body-centered cubic have been reported.[139] Transitioning to multicomponent systems, where complementary base pairings provide selective inter-LNP attraction/repulsion, has produced

a more diverse suite of morphologies such as the CsCl, AlB_2, Cr_3Si, and Cs_6C_{60} structures[138,140] (Fig. 5b). Application of these coarse-grained potentials to more complex DNA functionalized LNPs has also been successful at capturing the formation of low dimensional structures where small, mobile LNPs dynamically traverse the lattice to stabilize open lattice morphologies[141] (Fig. 5c).

Key takeaway. In addition to perturbation away from ideal LNPs with respect to the ligand length, the usage of DNA ligand incorporates how ligand architecture and attraction/repulsion influence both corona morphology and inter-LNP interactions. Stiff ligands (dsDNA) behave like hard ''sticky'' spheres while more flexible ligands (ssDNA) exhibit ''soft'' attractive sphere behaviors. Usage of dsDNA generally disfavors corona overlap due to high electrostatic repulsion and stiffness of the DNA double-helix. Conversely, ssDNA is more flexible but the negatively charged backbones create enough electrostatic repulsions between ligands that force the corona to lose some of its flexibility, pushing LNPs away from ''ultrasoft'' behaviors.

Long ligand functionalization on polyhedral NPs

To further increase LNP complexity, we now incorporate the effect of a polyhedral NP core in our discussion of oligomeric, polymer, and DNA ligands. Unlike spherical cores, where separate discussions are used for each ligand type, we combine discussion across ligand lengths using a governing theoretical model capable of predicting a continuous transition from hard to soft to ultrasoft corona morphologies in the limit of polyhedral core geometry.[79,99] This theory additionally extends to the limit of low surface coverage[48] and branching[99] or block copolymeric[142] ligand architectures.

Ligand functionalized polyhedral NPs – soft/ultrasoft shape interaction

Here, we assume that ligand functionalization falls within the high surface coverage regime. As such, the key feature that influences both corona morphology and emergent inter-LNP interactions lies in the interplay between local curvature and spatial confinement experienced by the functionalized ligands. As suggested by the corona morphologies observed in the spherical NP limit, there are three major regimes with respect to ligand spatial confinement that depend on the distance r_s from the NP surface: a rod-like limit at small r_s, a splaying/partially compressible limit at intermediate r_s, and an ultrasoft limit at large r_s. Unlike spherical LNPs, however, we must also consider how NP geometry influences the emergent corona morphology. Quantitatively, the effect of local curvature can be captured by first defining the size (R) of an anchored ligand as a function of relevant experimental parameters and surface position:[79]

$$R \sim R_{core}\sigma^{1/5}\nu^{1/5}b^{2/5}\left[\frac{N}{\Omega}\frac{b}{R_{core}}\right]^{3/5} \quad (9)$$

where N is the ligand length. The free energy of the chain is then simply: $\beta F \sim R^2/(Nb^2) + \nu N^2 f/(\Omega R)^3$ with $f = \sigma R_{core}{}^2$ and can be employed to compute a Boltzmann weighted probability of finding a ligand at any position on the NP surface. Inspection of eqn (9) indicates that the scaling exponent for N and Ω is the same, albeit inverse of each other. This means that we can view the ratio N/Ω as a composite parameter that defines an effective ligand length. High curvature surfaces such as edges/corners (high Ω) increase the local free volume available to the ligand, which ultimately decreases the net degree of ligand extension relative to the NP's low curvature locations. The net result is a lower free energy (βF), which provides an entropic driving force for ligand partitioning. Predictions of the average spatial distribution of ligands on NP cores of different geometries reveal three universal corona morphologies: conformal, convex, and concave coronas[79] (Fig. 6a).

Conformal coronas occur at short ligand lengths and are identical to the ''hard'' polyhedral LNPs discussed above. Convex coronas are the polyhedral analogues of ''soft'' spherical LNPs and occur at intermediate ligand lengths. The transition between these two regimes is identical to that discussed for ''hard'' polyhedral LNPs: $N \sim R_{core}\sigma^{1/2}\Omega^{-3/2}$. Here, the energy difference between ligands at high *versus* low curvature locations is small enough that the entropic partitioning force is on the order of thermal noise. This means that local chain fluctuations can offset the confinement energetic cost and thus ligands can stretch in place to reduce local confinement rather than undergoing surface partitioning. The net results are protruded spherical cap-like motifs at large faces on the NP surface, where there is a high degree of ligand stretching. Since the ligand stretching energy is on the order of thermal noise, interaction between neighboring convex coronas exhibits a moderate degree of ligand splaying and/or compression, reflective of the same phenomena observed in their ''soft'' spherical counterparts. Concave coronas are unique to polyhedral LNPs and arise due to a large gain in ligand conformational entropy associated with partitioning to edge/corner surface locations with minimal spatial confinement. This partitioning couples with a concurrent depletion of ligands from NP faces to produce the concave features intrinsic to this regime of corona phase space. The transition between a convex to concave corona happens at $N \sim R_{core}\sigma^{1/2}\Omega^{-3/2}\nu^{-1}$ or, analogously, when the ligand size is of the same size as the NP core size ($R_g \sim R_{core}$).

Since conformal coronas are identical to ''hard'' polyhedral LNPs, we refer the reader to the previous section for their computational modeling, effective inter-LNP interactions, and mapping of experimental handles to potential parameters. Convex and concave coronas, however, have no convenient effective functional forms with respect to inter-LNP potentials. Typically, these LNPs are modeled by first computing a potential of mean force (PMF) from simulation or self-consistent field calculations[79,99,143,144] and then fitting to any of the anisotropic variants of the above potentials for spherical LNPs (eqn (4)–(8)). An example set of computed PMF is shown in Fig. 6a for the particle configurations exhibiting the lowest interaction well-depth for each respective corona. The key aspect to note is that the emergent, optimal spatial and orientation

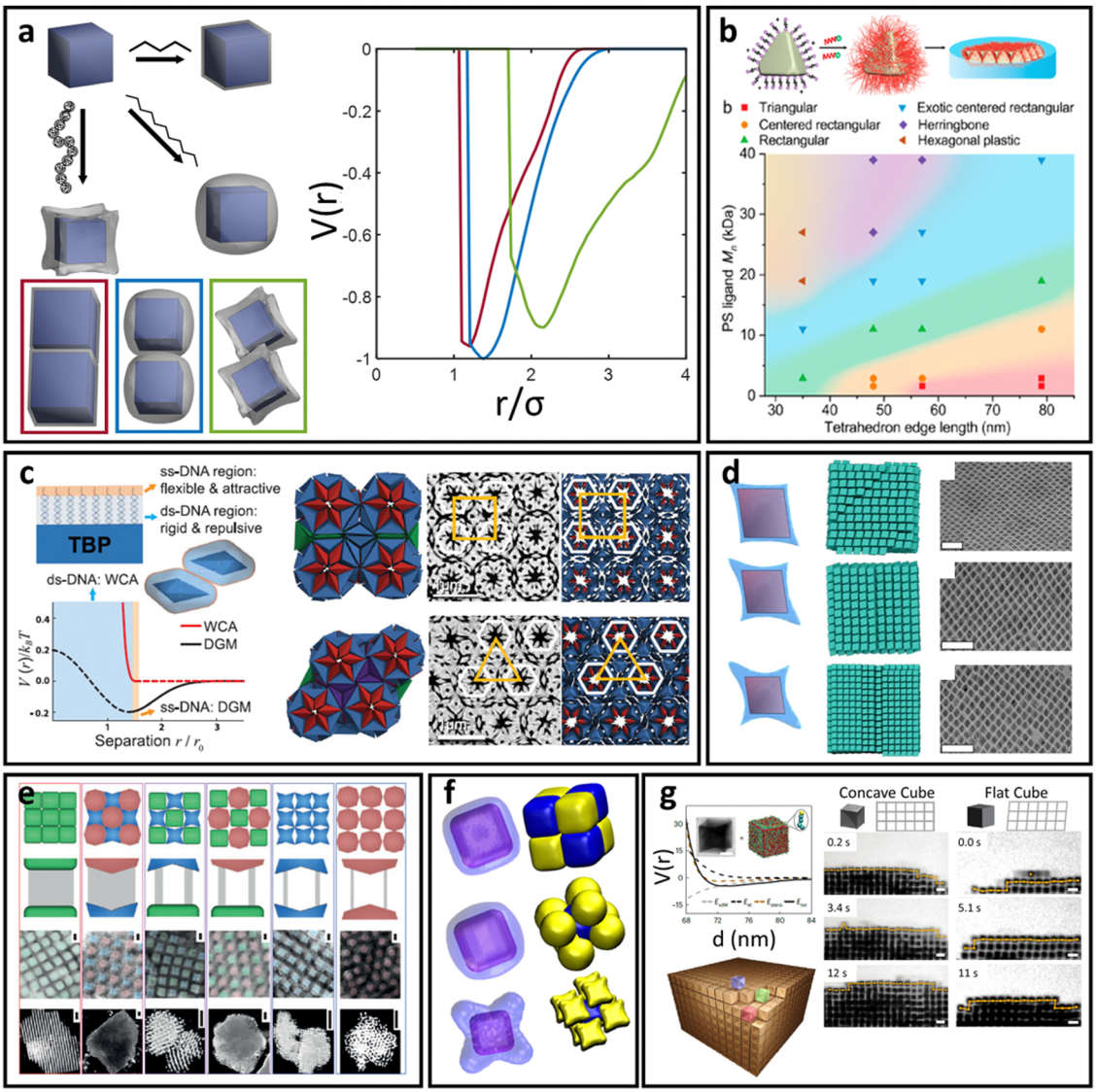

Fig. 6 "Soft" polyhedral LNPs. (a) Emergent interaction between ligand functionalized polyhedral NPs. The interplay between ligand confinement and NP surface curvature drives the formation of 3 distinct corona morphologies, each with distinct inter-LNP interactions: conformal (red), convex (blue), and concave (green). (b) Shift in corona morphology (due to the ligand length) can drive lattice transition in 2D assemblies of tetrahedral LNPs.[85] (c) DNA-functionalized bipyramids with conformal corona assemble into clathrate-like structures.[91] (d) Corona transition drives the formation of an off-set layer-by-layer stacking in nanoplates.[99] (e) Engineering corona shape complementarity can drive 3D close packed assembles.[146] For cubic NPs, (f) corona transition can drive unusual zig-zag orientational ordering[79] or (g) tune their assembly mechanisms.[147] Figures are reproduced from ref. 99 and 85 with permission from the American Chemical Society (© 2019 and 2022); ref. 91 and 79 with permission from the American Association for the Advancement of Science (© 2017 and 2019); and ref. 146 and 147 with permission from Springer Nature (© 2015 and 2023).

ordering between two anisotropic LNPs changes as a function of corona shape. In other words, LNP interactions are highly non-trivial and result from a combination of the interplay between ligand distribution, ligand lengths, and core geometry. This means that corona morphology must be computed before fitting/constructing the coarse-grained computational potential to ensure that the model correctly captures the spatial and orientational behaviors of these LNPs. Incorporating the effect of corona morphology in tuning LNP interactions has yielded a suite of pair potentials capable of capturing a diverse range of ligand functionalized polyhedral NP assemblies in both MC and MD simulations. Example core geometries include tetrahedra assembling into quasicrystalline structures[85,86] and closed/opened 2D packings[85] (Fig. 6b), bipyramids assembling into host–guest clathrate structures[90] (Fig. 6c), rhombuses that assemble into layer-by-layer square tiling[99] (Fig. 6d), cubes assembling into simple cubic and brick-wall tiling superlattices,[143,145] complementary coronas made using different NP core geometries that mediate close-packed 3D orderings[146] (Fig. 6e), octahedra that shift from simple hexagonal to Minkowski assemblies with increasing ligand lengths,[92] unusual zig-zag orientational organization of cubic NPs[79] (Fig. 6f), and co-assemblies of cubes and triangular nanoplates.[144] A recently published work has also expanded the application

of this protocol to predict the emergent corona morphology and interaction potentials for a wide range of complementary NP geometries that include truncated octahedra, cuboctahedra, bitetrahedra, and decahedra: all of which self-assemble into space-tiling superlattices.[92] Moreover, tuning corona morphology has been shown to provide a handle for control over the assembly mechanism of NP superlattices[147] (Fig. 6g).

Key takeaway. In summary, polyhedral LNPs deviate from the ideal limit in both ligand length and NP core geometry. Balancing the interplay between these two design handles gives rise to different classes of polyhedral LNP coronas that correspond to short, intermediate, and long ligand lengths. Of particular note is the formation of concave corona morphologies whose effective shapes deviate drastically from their underlying NP core. This indicates that ligand engineering can provide a powerful handle to design and control inter-LNP interactions between currently synthesizable NP geometry. Effective inter-LNP potentials for these complex corona morphologies are typically fitted to anisotropic variants of common isotropic pair potentials and then deployed in MC and MD simulations.

Ligand surface patterning on NPs – patchy interaction

As a final note, we discuss two LNP design handles that have been much less studied compared to those discussed in the previous sections: low surface coverage and ligand–ligand attraction. These two parameters work synergistically with each other to produce more exotic and orientationally specific LNP interactions. Examples of ligand–ligand attraction can include block copolymers that undergo microphase separation[55] or ligand aggregation due to exposure to a poor solvent.[148,149] Usage of sparse functionalization is often strategically chosen to allow for a high degree of ligand mobility so that ligand–ligand attraction does not result in kinetically trapped states within the corona. Similar to LNPs with polyhedral cores, there is an entropic driving force that governs ligand partitioning to high curvature locations. Ligand–ligand attractions introduce a counteracting enthalpic force that prevents ligand equipartitioning onto geometrically equivalent edges/corners. It is the interplay between these two opposing interactions that governs how ligands are organized on NP surfaces. In the entropically dominated regime, the emergent corona morphologies fall into one of the cases discussed above. However, in the enthalpically dominated regime, ligand distributions are highly non-ideal and often breaks the underlying NP core symmetry. Corona morphologies in this regime are predicted using modifications of eqn (9) to account for weak attraction between ligands,[48] leveraging microphase separation between block copolymeric ligands to produce surface partitioning[142] (Fig. 7c), or assuming a complete ligand collapse in the limit of poor solvent.[148,149] In general, the predicted coronas are patchy (*i.e.* localized to specific surface regions) and thus produce LNPs that exhibit directional interactions (Fig. 7a). Experimental realizations of patchy LNPs are still nascent and thus self-assembly of these systems beyond local clusters remains elusive. As such, computational modeling has been the prevalent tool for studying how emergent directionality in interactions drives LNP self-assembly.

In MC, an analytical potential developed specifically for patchy interactions is the Kern–Frenkel (KF) potential.[150] The KF potential is a generalization of the SW potential (eqn (7)) to account for directionality in interaction and has the form:

$$V_\theta\left(r,\hat{n}_i,\hat{n}_j\right) = \begin{cases} 1 & \text{if } \hat{n}_i\cdot\hat{r}_{ij} > \cos\theta \text{ and } \hat{n}_j\cdot\hat{r}_{ij} > \cos\theta \\ 0 & \text{otherwise} \end{cases}$$
$$V(r) = V_{\mathrm{SW}}(r)\,V_\theta\left(r,\hat{n}_i,\hat{n}_j\right) \tag{10}$$

where $V_{\mathrm{SW}}(r)$ defines the SW potential, $\hat{n}_i$ and $\hat{n}_j$ represent the unit direction of the patch on the ith and jth particle, respectively, and θ defines the opening angle of the patch. Qualitative mappings of experimental handles to potential parameters are: $\lambda \sim N^{2/5}$ defines the interpenetration ratio between interacting patches and $\varepsilon \sim N^{4/5}\sigma^{2/3}$ defines the mapping to effective LNP interaction strength. The core size a is simply the bare NP core size due to patchy grafts. Lastly, the opening angle θ depends on the patch size/shape and has been recently shown to scale[151] as $\sin\theta \sim N^{1/2}$. However, KF is limited to spherical/spheroidal particles. For patchy polyhedral LNPs, creating a polyhedral NP core particle modeled using an anisotropic potential (eqn (3)) that is then decorated with small spherical patches each exhibiting an attractive/repulsive Mie potential (eqn (4)) is the current state-of-the-art approach. Here, mapping the patch size to Mie parameters follows the same qualitative conversion discussed for oligomeric/polymeric ligands on spherical NPs. This approach has the additional benefit of being deployable in MD simulations due to the conservative nature of potentials applied to each subunit making up the entire patchy particle. Applications of such patchy potentials have resulted in a suite of interesting open lattices in simulations. Patchy rod particles are shown to self-assemble into the diamond lattice (Fig. 7b) – a holy grail for photonics applications.[152] KF-based patchy NPs can also self-assemble into helices,[153] honeycombed morphologies,[154] low density liquids,[155] clathrate-like structures,[156] and quasicrystalline morphologies[157] (Fig. 7d). Building upon the idea of breaking particle core symmetry, simulations of vertex-attractive concave triangular PNPs show that a porous, hexagonal lattice with uniform pore sizes can be achieved[158] (Fig. 7e). Additional simulations of such concave triangles reveal that the cores can encapsulate guest particles of varying shapes/sizes, making such PNPs ideal for the creation of porous materials with applications in separation or cargo encapsulation/transport.[159,160]

Key takeaway. Complex surface patterning in LNPs provides the largest perturbation away from the ideal LNP limit: (1) polyhedral core, (2) beyond steric repulsion between ligands on the same NP, and (3) sparse surface coverage. The emergent patchy LNP corona morphologies are a direct result of the delicate balance between these three counteracting parameters. The key takeaway here is that such a strategy can give rise to non-trivial coronas. Often, such coronas break the underlying symmetry of the NP core, allowing for unprecedented control over how LNPs

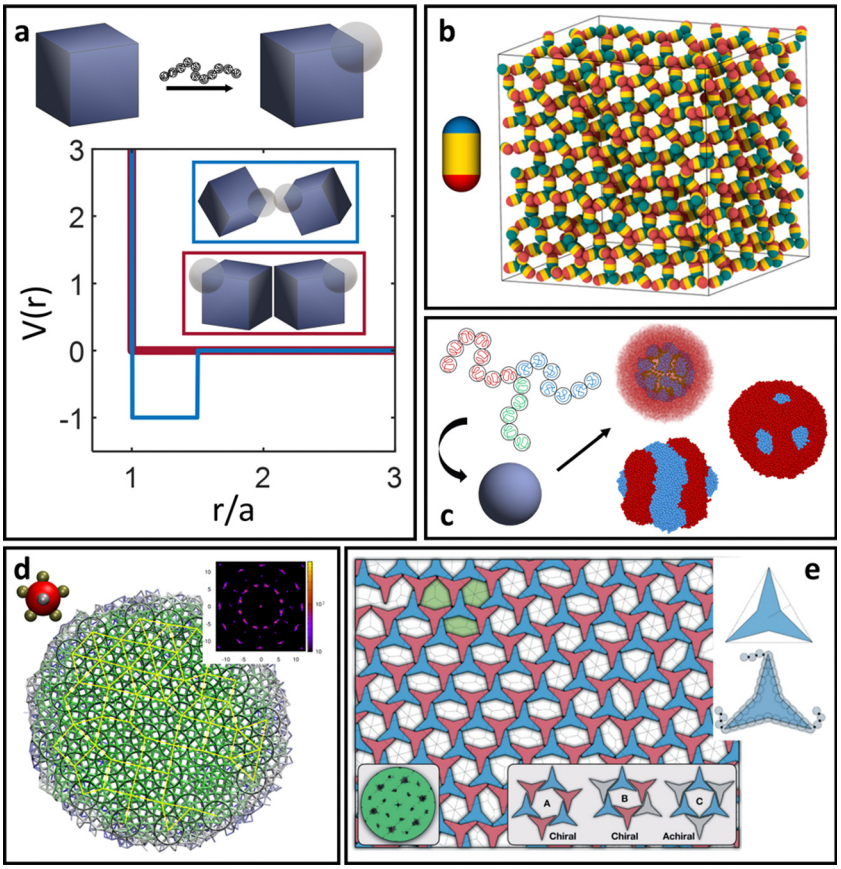

Fig. 7 Complex surface patterning of LNPs. (a) Emergent patchy/directional interactions between NPs with surface patterning. Examples of different types of patchy/patterning span a diverse suite of LNPs. (b) Simple diblock patchy ellipsoid self-assembles into a diamond lattice exhibiting a strong photonic band gap.[152] (c) Triblock polymer functionalization on NP surface leverages microphase separation to drive complex corona patterning.[142] (d) Self-assembly of a dodecagonal quasicrystal obtained from a pentagonal bipyramid patch configuration.[157] (e) Vertex patchy 2D concave triangles self-assemble into an open network structure exhibiting tunable, chiral pore structures.[158] Figures are reproduced from ref. 152 with permission from the American Chemical Society (© 2021); ref. 142 with permission from Wiley (© 2023); ref. 157 with permission from the American Institute of Physics (© 2021); and ref. 158 with permission from the Royal Society of Chemistry (© 2020).

are spatially and orientationally arranged within the resulting self-assembled structures.

To provide a quick reference for coarse-grain potential parameterization across the LNPs, we summarize the mapping between potential parameters for the various $V(r)$ (eqn (1)–(8) and (10)) discussed and experimental handles in Table 1. We note that these mappings are designed to match trends in interaction strengths, interaction ranges, and particle sizes as a function of experimental variables and are not meant to provide a direct correspondence between simulation and experiments. One-to-one conversions between experiments and coarse-grained potentials will necessitate direct measurements of PMFs or second virial coefficients (B_2) in experiments and fitting constants to the various potential parameters.

Theoretical prediction of LNP self-assembly

In addition to MC and MD simulations, the inter-LNP potentials discussed in the previous sections can be merged with theoretical tools designed for *a priori* prediction of LNP self-assembly. These tools typically quantify the free energy of LNPs when placed in a given spatial and orientational arrangement that corresponds to a candidate superlattice structure. Comparison across a suite of lattice configurations and selecting the one with the lowest free energy then provides a quantitative prediction of LNP self-assembly. Such approaches are extremely powerful in that they only utilize experimentally relevant parameters to characterize mesoscale level morphologies, providing a powerful handle for high throughput design of LNPs. Here, we split our discussion into "hard" *vs.* "soft" LNP self-assembly.

Theoretical prediction of "hard" LNP self-assembly

"Hard" LNPs are characterized by strong steric repulsions between neighboring particles. This means that entropy maximization provides the dominant driving force for LNP self-assembly. Since "hard" LNPs cannot overlap with each other, entropy maximization for these systems seeks configurations that minimize excluded volume between a reference particle and its neighbors.[100,101] Minimization of the effective volume

Table 1 Qualitative mapping between experimental parameters and coarse-grained (CG) potentials

Potential	Potential parameter	Experimental parameter	Ligand/NP type	Potential type	Applicability range
HS (eqn (1))	a	$N\sigma^{1/3}b$	Short ligand, spherical NPs	Hard spheres	$N \leq R_c\sigma^{1/2}$
WCA (eqn (2))	ε	$\sigma^{1/2}$			
	a	$N\sigma^{1/3}b$			
Hard shape (GJK + eqn (1))	a	$N\sigma^{1/3}b$	Short ligand, shaped NPs	Hard polyhedra	$N \leq R_c\frac{\sigma^{1/2}}{\Omega^{3/3}}$
Aniso-WCA (eqn (3))	ε	$\sigma^{1/2}$			
	a	$N\sigma^{1/3}b$			
Mie (eqn (4))	ε	$N^{1/2}\sigma^{1/2}$	Oligomeric ligand, polymeric ligand, DNA ligand, spherical/shaped NPs	Soft/ultrasoft spheres/polyhedra	$N > R_c\sigma^{1/2}$, $R_g < R_c$
	a	$N^{1/2}\sigma^{1/4}b$			
	$n - m$	$N^{-1/2}\sigma^{1/2}$			
Yukawa (eqn (5))	ε	$N^{4/5}\sigma^{2/3}$	Polymeric ligand, spherical/shaped NPs	Ultrasoft spheres/ polyhedra	$R_g \sim R_c$
	κ	$N^{3/5}\sigma^{1/5}b$			
OPP (eqn (6))	ε_1, ε_2	$N^{4/5}\sigma^{2/3}$			
	k, ϕ	$N^{3/5}\sigma^{1/5}b$			
Square well (eqn (7))	ε	$N_s\sigma$	dsDNA ligand, spherical/shaped NPs	Hard, selective spheres/polyhedra	—
	a	$N\sigma^{1/3}b$			
	λ	$1.25N_s$			
Square well (eqn (7))	ε	$N_s\sigma$	ssDNA ligand, spherical/shaped NPs	Soft, selective spheres/polyhedra	$N > R_c\sigma^{1/2}$
	a	$N_s^{3/5}\sigma^{1/5}b$			
	λ	$N_s^{2/5}$			
Fermi–Jagla (eqn (8))	ε, A_i, B_i	$N_s\sigma$			
	a	$N_s^{3/5}\sigma^{1/5}b$			
	n	$N_s^{-1/2}\sigma^{1/2}$			
Kern–Frenkel (eqn (10))	ε	$N^{4/5}\sigma^{2/3}$	Polymeric ligand, DNA ligand, spherical/shaped NPs	Patchy spheres/ polyhedra	$R_g \sim R_c$
	a	R_{core}			
	λ	$N^{2/3}$			
	θ	$\sin^{-1}(N^{1/2})$			

Variable definition: N: ligand degree of polymerization, σ: grafting density, b: ligand Kuhn length, R_{core}: NP radius (or insphere radius), R_g: ligand radius of gyration, and N_s: number of DNA "sticky-ends".

that a particle occupies within the lattice increases the space available to other particles, creating a large increase in translational entropy that drives LNP crystallization. For these reasons, seminal works on "hard" spherical LNPs assembly prediction over the past few decades have revolved around utilizing the packing fraction (η) as a proxy for the lattice free energy of formation. Specifically, structures that maximize η correspond to the thermodynamically equilibrium lattices. This approach has shown moderate successes with respect to common lattices such as face-centered cubic, body centered cubic, and Laves structures[161,162] (Fig. 8b). However, the packing fraction driven approach fails to capture more complex phases and often over predicts the range of lattice stability. Efforts to address this limitation have resulted in the inclusion of additional features such as emergent directionality/patchy interactions between closely packed LNP lattice prediction (Fig. 8a). Parameters such as nearest neighbor contacts, corona deformation, and corona overlap have all been utilized to define an effective packing fraction η_e. Here, η_e takes into account features such as how ligand splaying can give rise to partial corona overlaps between LNPs or how the coordination shell can produce emergent directional patchiness that slightly alters the LNP's excluded volume[163,164] (Fig. 8a). Of note is the recently developed Orbifold Topological Model, which has been shown to capture experimentally observed assembly behaviors across a wide range of "hard" LNP systems.[104,106,109]

With respect to "hard" polyhedral LNPs, a recently developed theory called entropic bonding (EBT)[165] has shown moderate successes in predicting both emergent directional interactions and the hierarchical self-assembly of hard polyhedra. Recognizing that excluded volume minimization drives entropic crystallization of "hard" polyhedral LNPs, EBT first quantifies the configuration between neighboring particles that minimizes their combined excluded volume. This is mapped to "shape orbitals" around a single polyhedron that indicates the emergent directional interaction between particles at high crowding (Fig. 8c). Through this lens, selecting particle configurations that maximize "shape orbital" overlap across all LNPs immediately results in system states with the lowest excluded volume and therefore the entropically stabilized lattices. Application of EBT to hard polyhedra self-assembly has successfully captured simple lattices such as simple cubic packing of cubes, Minkowski packing of octahedra, and face-centered cubic packing of spheres[165] (Fig. 8d). EBT even captures the formation of complex lattices such as clathrates,[90] host–guest structures,[93] layer-by-layer motifs,[94] and ultra-high density

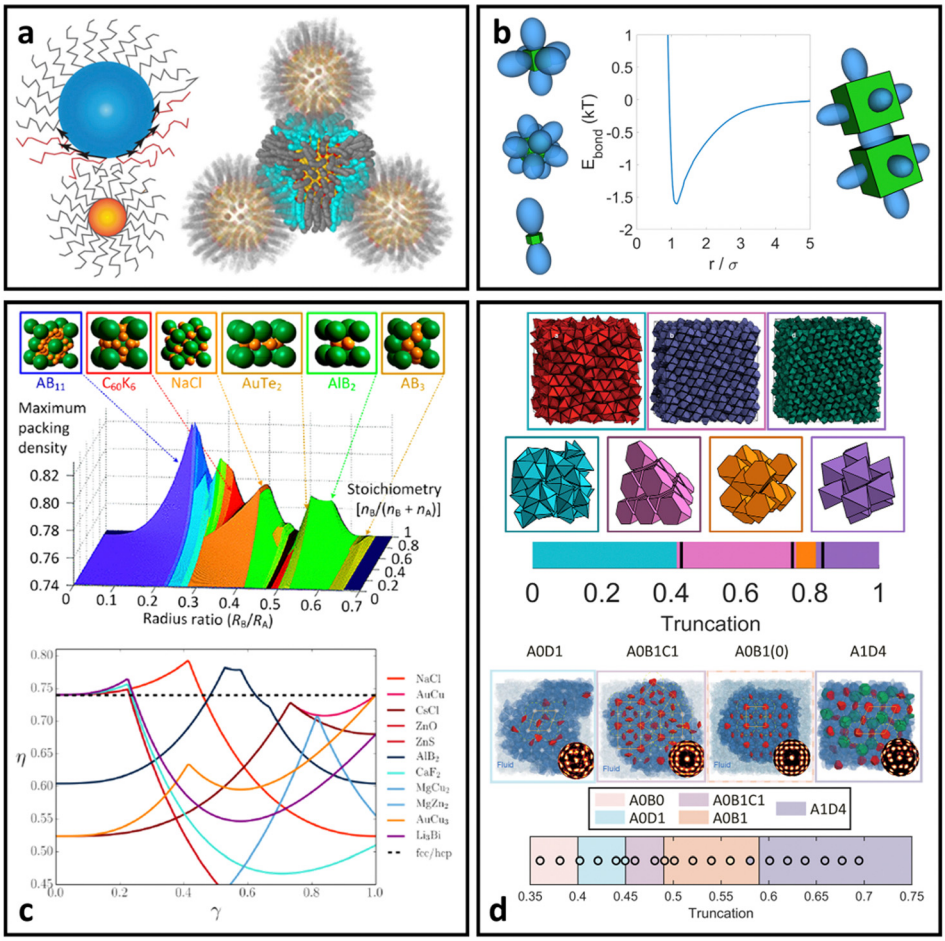

Fig. 8 "Hard" LNP self-assembly. (a) Ligand splaying and partial corona deformation between interacting hard spherical LNPs can alter local free volume and packing.[105,106] (b) Theoretical prediction of "hard" spherical LNPs relies on analysis of packing density and identifying structures with higher densities than FCC/HCP.[40,185] Corona splaying prediction from (a) extends the packing analysis to deformable coronas. (c) Directional interactions between "hard" polyhedral LNPs predicted *via* EBT.[165] (d) Application of EBT to predict a diverse suite of lattices ranging from simple cubic to clathrates to quasicrystals.[91,165,186] Figures are reproduced from ref. 186, 40 and 105 with permission from the American Chemical Society (© 2012, 2016, and 2021); ref. 106 with permission from the Royal Society of Chemistry (© 2016); ref. 185 with permission from the American Institute of Physics (© 2016); ref. 165 with permission from the National Academy of Sciences (© 2022); and ref. 91 with permission from the American Association for the Advancement of Science (© 2017).

packing of bipyramids[88] (Fig. 8d). It is important to note that the only required input into EBT is the intrinsic geometry of the particle shape. Emergent direction interactions, optimal particle orientation, and equilibrium spatial positions are all theoretically predicted from this input knowledge of particle geometry. Such simplicity in inputs makes EBT a powerful approach for both *a priori* prediction and design of "hard" polyhedral LNPs for hierarchical self-assembly.

Theoretical prediction of "soft" LNP self-assembly

"Soft" LNPs are characterized by the interplay between emergent inter-LNP attraction due to favorable corona overlap, steric hinderances arising from stretched ligands or NP core geometry, and species specific attraction/repulsion between ligands. In contrast to "hard" LNPs, assembly here is not governed by entropic maximization (*i.e.* particle packing) but rather by enthalpic minimization. To date, theories for "soft" LNP self-assembly have been built upon seminal works on Wertheim's thermodynamic perturbation theory (WTPT) for associating liquids.[166–170] Briefly, WTPT predicts the excess Helmholtz free energy of formation (A_{bond}) for spherically symmetric patchy particles interacting *via* the KF potential (eqn (10)), where A_{bond} takes the form:

$$\frac{A_{bond}}{MkT} = 2\ln X - X + 1$$

$$X = \frac{1}{1 + 2\rho X \Delta} \tag{11}$$

$$\Delta = 4\pi \int \langle f(r) \rangle_{\alpha} g_{HS}(r) r^2 dr$$

Here, ρ is the LNP number density, M is the number of LNPs, kT is the thermal energy, $g_{HS}(r)$ is the pair correlation function of a reference hard-sphere fluid, and $f(r)$ is the Mayer-f function: $f(r) = e^{-V(r)/kT} - 1$, where $V(r)$ defines the pairwise interaction potential between two LNPs (Fig. 9a, top). Applications of WTPT

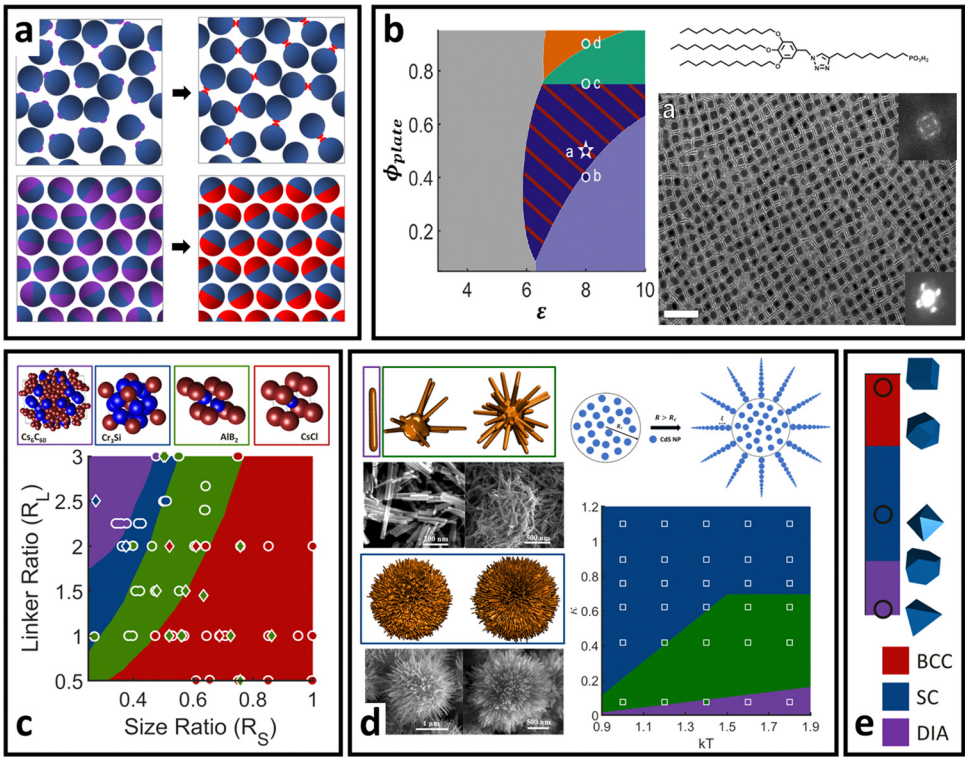

Fig. 9 "Soft" LNP self-assembly. (a) Schematic of generalization of WTPT from the hard sphere liquid reference state (top) to the hard sphere/polyhedral crystalline reference state (bottom). Application of this theory for "soft" PNDP is successful across a wide range of different types of nanoscale self-assembly. (b) Co-assembly of ligand functionalized nanocubes and nanoplates as a function of stoichiometry and interaction energy[144] (inverse temperature). (c) DNA-mediated spherical AuNP self-assembly.[178] (d) Electrostatics driven, self-limiting assembly of CdS supraparticles.[179] (e) Patchy DNA nanocage self-assembly showing transition from BCC to SC to a diamond superlattice with the changing core patchy shape.[177] All data points on the phase diagrams indicate experimental results and solid phases correspond to WTPT prediction. Figures are reproduced from ref. 144 with permission from the American Association for the Advancement of Science (© 2021); ref. 178 with permission from the National Academy of Sciences (© 2015); ref. 179 with permission from the American Chemical Society (© 2021); and ref. 177 with permission from Springer Nature (© 2020).

work extraordinarily well for predicting phase behaviors of PNP liquids ranging from vapor–liquid coexistence,[171] liquid–liquid phase separation,[155,172] ring formation,[173,174] gelation,[175] and binary/ternary systems.[176] While valid for the liquid state, eqn (11) cannot predict crystalline behaviors. To bridge WTPT to superlattice self-assembly, extensions have been made by recasting the reference pair correlation function, $g_{HS}(r)$, to that of a non-interacting, reference crystal: $g_{CR}(r)$. This yields a new form for:

$$\Delta = \prod_i \sum_j \frac{\rho^{s_{ij}}}{s_{ij}!} \int f_{ij}^{s_{ij}}(r) g_{ij,CR}(r) d\vec{r} \qquad (12)$$

where s is the coordination number of the perfect lattice and i and j define the types of interactions and particle types in the system, respectively[79,144,177] (Fig. 9a, bottom). Furthermore, eqn (12) removed the constraint of patchy particles by requiring that the input pair potential in $f(r)$ be for a particular set of relative particle orientations, generalizing its applicability to non-patchy particles and all the "soft" LNPs discussed earlier. This means that WTPT can now predict not only the thermodynamically stable equilibrium spatial configuration but also the optimal LNP orientations within the superlattice. Another advantage of eqn (12) is the dependence on a reference crystal. The workflow now becomes: (1) compute $g_{CR}(r)$ for a given guest lattice, (2) use eqn (12) to predict A_{bond}, (3) repeat across a suite of test lattices, and (4) select the lattice with the lowest A_{bond} as the thermodynamically stable structure. Eqn (12) is successful at *a priori* determining the equilibrium lattice structures across a range of systems that include ligand/oligomer-mediated[99,144] (Fig. 9b), DNA-mediated[79,178] (Fig. 9c), chiral/electrostatics-mediated[179,180] (Fig. 9d), DNA nanocage[177] (Fig. 9e), and evaporation-driven[53] self-assembly, all of which have been validated by experiments. As a final note, we emphasize that all previously discussed emergent interactions for LNPs (Table 1) provide approximations for $V(r)$ to use in eqn (12). This general feature of WTPT makes it readily applicable across all LNP systems discussed throughout this review. To summarize the large diversity of structures accessible using LNPs, we organize the structural space of LNP self-assembly in Fig. 10 as a function of LNP complexity (*i.e.* hard, soft, ultrasoft, patchy, *etc.*) and system complexity (*i.e.* single component or multi-component).

Conclusion and outlook on new directions for LNPs

Despite the unprecedented growth in our ability to synthesize, model, and predict LNP self-assembly, key challenges remain.

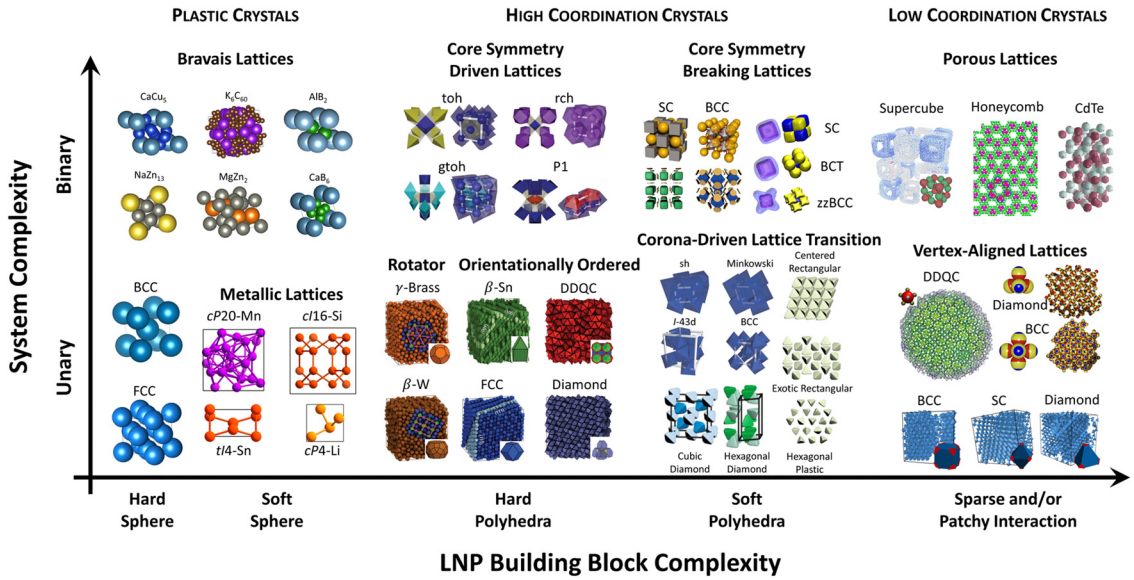

Fig. 10 Structural diversity in LNP self-assembly. Schematic of assembly morphologies for LNPs as a function of building block and system complexity phase space. Snapshots indicate classes of structural organizations accessible for each phase space regime and do not reflect the entire space of all accessible assembled morphologies. Abbreviations utilized are: body-centered cubic (BCC), face-centered cubic (FCC), simple cubic (SC), body-centered tetragonal (BCT), zig-zag oriented BCC (zzBCC), tetra-octa honeycomb (toh), gyrated tetra-octa honeycomb (gtoh), rectified cubic honeycomb (rch), Penrose P1 tiling (P1), simple hexagonal (sh), and dodecagonal quasicrystal (DDQC). The figure contains images reproduced from ref. 83, 85, 92, 116, 142, 146, 177, 187–189; ref. 83 and 92 with permission from the American Association for the Advancement of Science (© 2012 and 2024); ref. 116 with permission from the National Academy of Sciences (© 2021); ref. 142 with permission from Wiley (© 2023); ref. 146, 177 and 187 with permission from Springer Nature (© 2015 and 2020); and ref. 188, 85 and 189 with permission from the American Chemical Society (© 2018, 2022, and 2023).

Firstly, as demands for precision control over inter-LNP interactions increase, more advanced methods are needed to increase surface selectivity in ligand functionalization. Increased precision, however, presents major challenges for synthesis[48,181] as LNP surface patterning is constrained by the intrinsic core NP geometry. Development of new theory and computational tools to guide experiments is critical as the number of potential design parameters is too large for a brute force "trial-and-error" approach.

Secondly, the advent of patchy LNPs resulting from complex LNP surface patterning has also opened newer avenues for stringing together LNPs into long chains *via* patch–patch interactions.[151] These "colloidal" polymers have been shown to exhibit strong plasmonic responses, making them ideal for applications in creating next-generation sensors. Unlike traditional polymers, however, each monomer here is an entire LNP with well-defined and unique geometry. Little work has been done on looking at how these geometrical effects influence chain conformation and packing, making *a priori* design of "colloidal" chains to target specific modes of plasmonic responses an on-going challenge.

Thirdly, due to the increased complexity of experimentally accessible LNP building blocks used in self-assembly, the likelihood of kinetic traps during assembly has also dramatically increased. As a result, assembly pathway engineering that explicitly accounts for both LNP softness and directional interactions is also of interest. Questions that will be relevant to answer here are: (1) what is the hierarchy of motifs needed to achieve the final self-assembled structures? (2) how does one assembly pathway reduce the potential for kinetic traps relative to another? and (3) how do rotational and translation dynamics of the highly anisotropic LNPs influence the assembly pathway? Answering these questions not only builds a more fundamental understanding of the complex behaviors underlying LNP assemblies but also provides critical insights into design strategies to develop more novel assembly structures.

In short, the design and synthesis of polymer/DNA functionalized nanoparticles is an exciting field with incredible promise for applications in catalysis, sensing, soft robotics, and energy harvesting. Our review covers the current state-of-the-art computational and theoretical approaches to modeling and predicting how ligand functionalization can imbue complex, emergent interactions between nanoparticles that can sometime break the intrinsic geometry of their constitutive parts. Key developments in fundamental understanding of how ligands are organized when functionalized onto NP surfaces have not only expanded our understanding of assembly physics but also enabled powerful approaches for inverse design of LNPs to develop a wide range of different superlattices with applications spanning across all technologically relevant fields in nanoscience. Altogether, these results suggest that the future of LNP synthesis and self-assembly is bright. Thanks to the chemical diversity of both ligand types and NP core geometry, LNPs present a class of nanoscale synthons capable of realizing complex building blocks for use in creating multifunctional and ordered materials at the mesoscale and beyond.

Author contributions

T. V. led the manuscript development and wrote the manuscript.

Conflicts of interest

The authors declare no conflicts of interest.

Acknowledgements

T. V. thanks the Ralph E. Powe Junior Faculty Enhancement Award for partial financial support of this work.

References

1 H. A. Nguyen, G. Dixon, F. Y. Dou, S. Gallagher, S. Gibbs, D. M. Ladd, E. Marino, J. C. Ondry, J. P. Shanahan, E. S. Vasileiadou, S. Barlow, D. R. Gamelin, D. S. Ginger, D. M. Jonas, M. G. Kanatzidis, S. R. Marder, D. Morton, C. B. Murray, J. S. Owen, D. V. Talapin, M. F. Toney and B. M. Cossairt, *Chem. Rev.*, 2023, **123**, 7890–7952.
2 N. H. Cho, A. Guerrero-Martínez, J. Ma, S. Bals, N. A. Kotov, L. M. Liz-Marzán and K. T. Nam, *Nat. Rev. Bioeng.*, 2023, **1**, 88–106.
3 J. Crassous, M. J. Fuchter, D. E. Freedman, N. A. Kotov, J. Moon, M. C. Beard and S. Feldmann, *Nat. Rev. Mater.*, 2023, **8**, 365–371.
4 C. R. Kagan, L. C. Bassett, C. B. Murray and S. M. Thompson, *Chem. Rev.*, 2021, **121**, 3186–3233.
5 Y. Wu, J. Feng, Z. Yang, Y. Liu, S. Liu, Y. Wu, J. Feng, Z. Yang, Y. Liu and S. Liu, *Adv. Sci.*, 2023, **10**, 2205536.
6 P. C. Y. Chow, T. Someya, P. C. Y. Chow and T. Someya, *Adv. Mater.*, 2020, **32**, 1902045.
7 J. Plocher and A. Panesar, *Mater. Des.*, 2019, **183**, 108164.
8 R. Kumar, S. Sahoo, E. Joanni, R. K. Singh, W. K. Tan, K. K. Kar and A. Matsuda, *Prog. Energy Combust. Sci.*, 2019, **75**, 100786.
9 C. Liu, H. Chen, S. Wang, Q. Liu, Y. G. Jiang, D. W. Zhang, M. Liu and P. Zhou, *Nat. Nanotechnol.*, 2020, **15**, 545–557.
10 J. H. Swisher, L. Jibril, S. H. Petrosko and C. A. Mirkin, *Nat. Rev. Mater.*, 2022, **7**, 428–448.
11 K. M. Herbert, S. Schrettl, S. J. Rowan and C. Weder, *Macromolecules*, 2017, **50**, 8845–8870.
12 T. M. Swager, *Macromolecules*, 2017, **50**, 4867–4886.
13 T. P. Russell and Y. Chai, *Macromolecules*, 2017, **50**, 4597–4609.
14 Y. Zhang and S. J. Park, *Polymers*, 2019, **11**, 909.
15 T. Ray, J. Choi, J. Reeder, S. P. Lee, A. J. Aranyosi, R. Ghaffari and J. A. Rogers, *Curr. Opin. Biomed. Eng.*, 2019, **9**, 47–56.
16 G. H. Lee, H. Moon, H. Kim, G. H. Lee, W. Kwon, S. Yoo, D. Myung, S. H. Yun, Z. Bao and S. K. Hahn, *Nat. Rev. Mater.*, 2020, **5**, 149–165.
17 Y. Zhang, D. Kim, R. Dong, X. Feng and C. O. Osuji, *Sci. Adv.*, 2022, **8**, 5899.
18 J. W. Barnett, C. R. Bilchak, Y. Wang, B. C. Benicewicz, L. A. Murdock, T. Bereau and S. K. Kumar, *Sci. Adv.*, 2020, **6**, 1–7.
19 X. Li, G. Jiang, M. Jian, C. Zhao, J. Hou, A. W. Thornton, X. Zhang, J. Z. Liu, B. D. Freeman, H. Wang, L. Jiang and H. Zhang, *Nat. Commun.*, 2023, **14**, 1–12.
20 P. R. Kidambi, P. Chaturvedi and N. K. Moehring, *Science*, 2021, **374**, 1–12.
21 M. C. Ferrari, *Curr. Opin. Chem. Eng.*, 2023, **40**, 100905.
22 M. Galizia, W. S. Chi, Z. P. Smith, T. C. Merkel, R. W. Baker and B. D. Freeman, *Macromolecules*, 2017, **50**, 7809–7843.
23 D. T. Lee, P. Corkery, S. Park, H. K. Jeong and M. Tsapatsis, *Ann. Rev. Chem. Biomol. Eng.*, 2022, **13**, 529–555.
24 Y. Fu, Y. B. Jiang, D. Dunphy, H. Xiong, E. Coker, S. Chou, H. Zhang, J. M. Vanegas, J. G. Croissant, J. L. Cecchi, S. B. Rempe and C. J. Brinker, *Nat. Commun.*, 2018, **9**, 1–12.
25 A. Cangialosi, C. K. Yoon, J. Liu, Q. Huang, J. Guo, T. D. Nguyen, D. H. Gracias and R. Schulman, *Science*, 2017, **357**, 1126–1130.
26 A. Pantula, B. Datta, Y. Shi, M. Wang, J. Liu, S. Deng, N. J. Cowan, T. D. Nguyen and D. H. Gracias, *Sci. Robot.*, 2022, **7**, 1–10.
27 G. M. Whitesides, *Angew. Chem., Int. Ed.*, 2018, **57**, 4258–4273.
28 S. Lee, H. A. Calcaterra, S. Lee, W. Hadibrata, B. Lee, E. B. Oh, K. Aydin, S. C. Glotzer and C. A. Mirkin, *Nature*, 2022, **610**, 674–679.
29 M. Annadhasan, S. Basak, N. Chandrasekhar, R. Chandrasekar, M. Annadhasan, S. Basak, N. Chandrasekhar and R. Chandrasekar, *Adv. Opt. Mater.*, 2020, **8**, 2000959.
30 G. A. Ermolaev, D. V. Grudinin, Y. V. Stebunov, K. V. Voronin, V. G. Kravets, J. Duan, A. B. Mazitov, G. I. Tselikov, A. Bylinkin, D. I. Yakubovsky, S. M. Novikov, D. G. Baranov, A. Y. Nikitin, I. A. Kruglov, T. Shegai, P. Alonso-González, A. N. Grigorenko, A. V. Arsenin, K. S. Novoselov and V. S. Volkov, *Nat. Commun.*, 2021, **12**, 1–8.
31 M. S. Ergoktas, G. Bakan, E. Kovalska, L. W. Le Fevre, R. P. Fields, P. Steiner, X. Yu, O. Salihoglu, S. Balci, V. I. Fal'ko, K. S. Novoselov, R. A. W. Dryfe and C. Kocabas, *Nat. Photonics*, 2021, **15**, 493–498.
32 Y. Li and J. Yu, *Nat. Rev. Mater.*, 2021, **6**, 1156–1174.
33 E. L. Bell, W. Finnigan, S. P. France, A. P. Green, M. A. Hayes, L. J. Hepworth, S. L. Lovelock, H. Niikura, S. Osuna, E. Romero, K. S. Ryan, N. J. Turner and S. L. Flitsch, *Nat. Rev. Methods Primers*, 2021, **1**, 1–21.
34 R. Verduzco, X. Li, S. L. Pesek and G. E. Stein, *Chem. Soc. Rev.*, 2015, **44**, 2405–2420.
35 E. V. Amadi, A. Venkataraman and C. Papadopoulos, *Nanotechnology*, 2022, **33**, 132001.
36 L. Cademartiri and K. J. M. Bishop, *Nat. Mater.*, 2014, **14**, 2–9.
37 S. A. Mallory, C. Valeriani and A. Cacciuto, *Annu. Rev. Phys. Chem.*, 2018, **69**, 59–79.
38 Z. Li, Q. Fan and Y. Yin, *Chem. Rev.*, 2022, **122**, 4976–5067.

39 M. Dwivedi, S. L. Singh, A. S. Bharadwaj, V. Kishore and A. V. Singh, *Micromachines*, 2022, **13**, 1–18.
40 M. A. Boles, M. Engel and D. V. Talapin, *Chem. Rev.*, 2016, **116**, 11220–11289.
41 U. Tritschler, S. Pearce, J. Gwyther, G. R. Whittell and I. Manners, *Macromolecules*, 2017, **50**, 3439–3463.
42 E. V. Shevchenko, D. V. Talapin, N. A. Kotov, S. O'Brien and C. B. Murray, *Nature*, 2006, **439**, 55–59.
43 J. Henzie, M. Grünwald, A. Widmer-Cooper, P. L. Geissler and P. Yang, *Nat. Mater.*, 2011, **11**, 131–137.
44 J. S. Kahn and O. Gang, *Angew. Chem., Int. Ed.*, 2022, **61**, e202105678.
45 C. A. Mirkin and S. H. Petrosko, *ACS Nano*, 2023, **17**, 16291–16307.
46 Y. J. Kim, J. H. Kim, I. S. Jo, D. J. Pine, S. Sacanna and G. R. Yi, *J. Am. Chem. Soc.*, 2021, **143**, 13175–13183.
47 K. H. Ku, Y. J. Kim, G. R. Yi, Y. S. Jung and B. J. Kim, *ACS Nano*, 2015, **9**, 11333–11341.
48 A. Kim, T. Vo, H. An, P. Banerjee, L. Yao, S. Zhou, C. Kim, D. J. Milliron, S. C. Glotzer and Q. Chen, *Nat. Commun.*, 2022, **13**, 1–14.
49 J. A. A. Diaz, J. S. Oh, G. R. Yi and D. J. Pine, *Proc. Natl. Acad. Sci. U. S. A.*, 2020, **117**, 10645–10653.
50 S. Stuij, J. Rouwhorst, H. J. Jonas, N. Ruffino, Z. Gong, S. Sacanna, P. G. Bolhuis and P. Schall, *Phys. Rev. Lett.*, 2021, **127**, 108001.
51 E. Marino, S. W. Van Dongen, S. J. Neuhaus, W. Li, A. W. Keller, C. R. Kagan, T. E. Kodger and C. B. Murray, *Chem. Mater.*, 2022, **34**, 2779–2789.
52 H. Joukhdar, A. Seifert, T. Jüngst, J. Groll, M. S. Lord, J. Rnjak-Kovacina, H. Joukhdar, A. M. S. Lord, J. Rnjak-Kovacina, Au. A. Seifert, T. Jüngst and J. Groll, *Adv. Mater.*, 2021, **33**, 2100091.
53 K. C. Elbert, T. Vo, D. Oh, H. Bharti, S. C. Glotzer and C. B. Murray, *ACS Nano*, 2022, **16**, 4508–4516.
54 C. M. Bates and F. S. Bates, *Macromolecules*, 2017, **50**, 3–22.
55 F. S. Bates and G. H. Fredrickson, *Annu. Rev. Phys. Chem.*, 2003, **41**, 525–557.
56 S. C. Glotzer and M. J. Solomon, *Nat. Mater.*, 2007, **6**, 557–562.
57 M. R. Jones, N. C. Seeman and C. A. Mirkin, *Science*, 2015, **347**, 1260901.
58 D. Samanta, W. Zhou, S. B. Ebrahimi, S. H. Petrosko and C. A. Mirkin, *Adv. Mater.*, 2022, **34**, 2107875.
59 Z. G. Wang, *Macromolecules*, 2017, **50**, 9073–9114.
60 J. D. Weeks, D. Chandler and H. C. Andersen, *J. Chem. Phys.*, 1971, **54**, 5237–5247.
61 B. J. Alder and T. E. Wainwright, *J. Chem. Phys.*, 1957, **27**, 1208–1209.
62 I. Borukhov and L. Leibler, *Macromolecules*, 2002, **35**, 5171–5182.
63 J. J. Erpenbeck and W. W. Wood, *J. Stat. Phys.*, 1984, **35**, 321–340.
64 H. N. W. Lekkerkerker and R. Tuinier, *Lecture Notes Phys.*, 2011, **833**, 109–129.
65 W. W. Wood and J. D. Jacobson, *J. Chem. Phys.*, 1957, **27**, 1207–1208.
66 J. A. Barker and D. Henderson, *Mol. Phys.*, 1971, **21**, 187–191.
67 J. Zhu, M. Li, R. Rogers, W. Meyer, R. H. Ottewill, W. B. Russel and P. M. Chaikin, *Nature*, 1997, **387**, 883–885.
68 P. K. Bommineni, N. R. Varela-Rosales, M. Klement and M. Engel, *Phys. Rev. Lett.*, 2019, **122**, 128005.
69 Y. Zhou and G. Arya, *Nat. Commun.*, 2022, **13**, 1–12.
70 E. Fayen, L. Filion, G. Foffi and F. Smallenburg, *Phys. Rev. Lett.*, 2024, **132**, 048202.
71 S. Jiménez-Millán, C. García-Alcántara, A. Ramírez-Hernández, E. J. Sambriski and S. I. Hernández, *J. Mol. Liq.*, 2021, **335**, 116219.
72 D. Wang, T. Dasgupta, E. B. van der Wee, D. Zanaga, T. Altantzis, Y. Wu, G. M. Coli, C. B. Murray, S. Bals, M. Dijkstra and A. van Blaaderen, *Nat. Phys.*, 2020, **17**, 128–134.
73 J. Wang, C. F. Mbah, T. Przybilla, S. Englisch, E. Spiecker, M. Engel and N. Vogel, *ACS Nano*, 2019, **13**, 9005–9015.
74 M. P. Allen, D. Frenkel and J. Talbot, *Comput. Phys. Rep.*, 1989, **9**, 301–353.
75 S. Hess, M. Kröger and H. Voigt, *Phys. A*, 1998, **250**, 58–82.
76 J. Jin, K. S. Schweizer and G. A. Voth, *J. Chem. Phys.*, 2023, **158**, 034104.
77 E. J. Saltzman and K. S. Schweizer, *J. Chem. Phys.*, 2006, **125**, 44509.
78 P. K. Bommineni, M. Klement and M. Engel, *Phys. Rev. Lett.*, 2020, **124**, 218003.
79 F. Lu, T. Vo, Y. Zhang, A. Frenkel, K. G. Yager, S. Kumar and O. Gang, *Sci. Adv.*, 2019, **5**, 2399–2416.
80 E. G. Gilbert, D. W. Johnson and S. S. Keerthi, *IEEE J. Rob. Automation*, 1988, **4**, 193–203.
81 M. Sagardia, T. Stouraitis and J. Lopes e Silva, 11th Conference and Exhibition of the European Association of Virtual Reality and Augmented Reality, EuroVR 2014, 2014, pp. 65–76.
82 U. Agarwal and F. A. Escobedo, *Nat. Mater.*, 2011, **10**, 230–235.
83 P. F. Damasceno, M. Engel and S. C. Glotzer, *Science*, 2012, **337**, 453–457.
84 A. P. Gantapara, J. De Graaf, R. Van Roij and M. Dijkstra, *Phys. Rev. Lett.*, 2013, **111**, 015501.
85 Y. Wang, J. Chen, Y. Zhong, S. Jeong, R. Li and X. Ye, *J. Am. Chem. Soc.*, 2022, **144**, 13538–13546.
86 Y. Wang, J. Chen, R. Li, A. Götz, D. Drobek, T. Przybilla, S. Hübner, P. Pelz, L. Yang, B. Apeleo Zubiri, E. Spiecker, M. Engel and X. Ye, *J. Am. Chem. Soc.*, 2023, **145**, 17902–17911.
87 X. Ye, J. Chen, M. Engel, J. A. Millan, W. Li, L. Qi, G. Xing, J. E. Collins, C. R. Kagan, J. Li, S. C. Glotzer and C. B. Murray, *Nat. Chem.*, 2013, **5**, 466–473.
88 A. Haji-Akbari, M. Engel and S. C. Glotzer, *Phys. Rev. Lett.*, 2011, **107**, 215702.
89 A. Haji-Akbari, M. Engel, A. S. Keys, X. Zheng, R. G. Petschek, P. Palffy-Muhoray and S. C. Glotzer, *Nature*, 2009, **462**, 773–777.

90 S. Lee, T. Vo and S. C. Glotzer, *Nat. Chem.*, 2023, **15**, 905–912.
91 H. Lin, S. Lee, L. Sun, M. Spellings, M. Engel, S. C. Glotzer and C. A. Mirkin, *Science*, 2017, **355**, 931–935.
92 W. Zhou, Y. Li, K. Je, T. Vo, H. Lin, B. E. Partridge, Z. Huang, S. C. Glotzer and C. A. Mirkin, *Science*, 2024, **383**, 312–319.
93 T. C. Moore, J. A. Anderson and S. C. Glotzer, *Soft Matter*, 2021, **17**, 2840–2848.
94 S. Lee, E. G. Teich, M. Engel and S. C. Glotzer, *Proc. Natl. Acad. Sci. U. S. A.*, 2019, **116**, 14843–14851.
95 M. P. Allen and G. Germano, *Mol. Phys.*, 2006, **104**, 3225–3235.
96 M. Spellings, R. L. Marson, J. A. Anderson and S. C. Glotzer, *J. Comput. Phys.*, 2017, **334**, 460–467.
97 B. H. J. Lee and G. Arya, *Nanoscale Horiz.*, 2020, **5**, 1628–1642.
98 V. Ramasubramani, T. Vo, J. A. Anderson and S. C. Glotzer, *J. Chem. Phys.*, 2020, **153**, 084106.
99 K. C. Elbert, T. Vo, N. M. Krook, W. Zygmunt, J. Park, K. G. Yager, R. J. Composto, S. C. Glotzer and C. B. Murray, *ACS Nano*, 2019, **13**, 14241–14251.
100 D. Frenkel, *Phys. A*, 1999, **263**, 26–38.
101 D. Frenkel, *Nat. Mater.*, 2014, **14**, 9–12.
102 L. Onsager, *Ann. N. Y. Acad. Sci.*, 1949, **51**, 627–659.
103 Y. Wang, P. J. Santos, J. M. Kubiak, X. Guo, M. S. Lee and R. J. Macfarlane, *J. Am. Chem. Soc.*, 2019, **141**, 13234–13243.
104 A. Travesset, *ACS Nano*, 2017, **11**, 5375–5382.
105 X. Zha and A. Travesset, *J. Phys. Chem. C*, 2021, **125**, 18936–18945.
106 A. Travesset, *Soft Matter*, 2016, **13**, 147–157.
107 D. Meng, S. K. Kumar, J. M. D. Lane and G. S. Grest, *Soft Matter*, 2012, **8**, 5002–5010.
108 C. Waltmann, N. Horst and A. Travesset, *J. Chem. Phys.*, 2018, **149**, 34109.
109 I. Cherniukh, T. V. Sekh, G. Rainò, O. J. Ashton, M. Burian, A. Travesset, M. Athanasiou, A. Manoli, R. A. John, M. Svyrydenko, V. Morad, Y. Shynkarenko, F. Montanarella, D. Naumenko, H. Amenitsch, G. Itskos, R. F. Mahrt, T. Stöferle, R. Erni, M. V. Kovalenko and M. I. Bodnarchuk, *ACS Nano*, 2021, **16**, 2024.
110 A. Upah, A. Thomas, J. Hallstrom and A. Travesset, *J. Chem. Theory Comput.*, 2024, **20**, 1559–1567.
111 J. J. Potoff and D. A. Bernard-Brunel, *J. Phys. Chem. B*, 2009, **113**, 14725–14731.
112 E. Marino, R. A. LaCour, T. C. Moore, S. W. van Dongen, A. W. Keller, D. An, S. Yang, D. J. Rosen, G. Gouget, E. H. R. Tsai, C. R. Kagan, T. E. Kodger, S. C. Glotzer and C. B. Murray, *Nat. Synth.*, 2023, **3**, 111–122.
113 M. Daoud and J. P. Cotton, *J. Phys.*, 1982, **43**, 531–538.
114 R. A. Lacour, C. S. Adorf, J. Dshemuchadse and S. C. Glotzer, *ACS Nano*, 2019, **13**, 13829–13842.
115 R. A. Lacour, T. C. Moore and S. C. Glotzer, *Phys. Rev. Lett.*, 2022, **128**, 188001.
116 J. Dshemuchadse, P. F. Damasceno, C. L. Phillips, M. Engel and S. C. Glotzer, *Proc. Natl. Acad. Sci. U. S. A.*, 2021, **118**, e2024034118.
117 W. L. Chen, R. Cordero, H. Tran and C. K. Ober, *Macromolecules*, 2017, **50**, 4089–4113.
118 S. T. Milner, *Science*, 1991, **251**, 905–914.
119 C. Ligoure and L. Leibler, *Macromolecules*, 1990, **23**, 5044–5046.
120 K. Ohno, T. Morinaga, S. Takeno, Y. Tsujii and T. Fukuda, *Macromolecules*, 2007, **40**, 9143–9150.
121 J. Midya, M. Rubinstein, S. K. Kumar and A. Nikoubashman, *ACS Nano*, 2020, **14**, 15505–15516.
122 R. Menichetti and A. Pelissetto, *J. Chem. Phys.*, 2013, **138**, 124902.
123 C. N. Likos, H. Löwen, M. Watzlawek, B. Abbas, O. Jucknischke, J. Allgaier and D. Richter, *Phys. Rev. Lett.*, 1998, **80**, 4450.
124 T. Lafitte, S. K. Kumar and A. Z. Panagiotopoulos, *Soft Matter*, 2014, **10**, 786–794.
125 Z. Wu, S. Pal and S. Keten, *Macromolecules*, 2023, **56**, 3259–3271.
126 M. Asai, A. Cacciuto and S. K. Kumar, *Soft Matter*, 2014, **11**, 793–797.
127 J. U. Kim and M. W. Matsen, *Macromolecules*, 2008, **41**, 4435–4443.
128 T. A. Witten, P. A. Pincus and P. A. Pincus, *Macromolecules*, 1986, **19**, 2509–2513.
129 M. M. Marques, T. P. O. Nogueira, R. F. Dillenburg, M. C. Barbosa and J. R. Bordin, *J. Appl. Phys.*, 2020, **127**, 54701.
130 K. Binder and A. Milchev, *J. Polym. Sci., Part B: Polym. Phys.*, 2012, **50**, 1515–1555.
131 K. J. Modica, T. B. Martin and A. Jayaraman, *Macromolecules*, 2017, **50**, 4854–4866.
132 C. Koh, G. S. Grest and S. K. Kumar, *ACS Nano*, 2020, **14**, 13491–13499.
133 H. Yukawa, *Prog. Theor. Phys. Suppl.*, 1955, **1**, 1–10.
134 J. P. K. Doye, D. J. Wales and S. I. Simdyankin, *Faraday Discuss.*, 2001, **118**, 159–170.
135 J. Bednar, P. Furrer, V. Katritch, A. Z. Stasiak, J. Dubochet and A. Stasiak, *J. Mol. Biol.*, 1995, **254**, 579–594.
136 Z. Ovanesyan, B. Medasani, M. O. Fenley, G. I. Guerrero-García, M. O. De La Cruz and M. Marucho, *J. Chem. Phys.*, 2014, **141**, 225103.
137 J. A. Barker and D. Henderson, *J. Chem. Phys.*, 1967, **47**, 2856–2861.
138 E. Pretti, H. Zerze, M. Song, Y. Ding, N. A. Mahynski, H. W. Hatch, V. K. Shen and J. Mittal, *Soft Matter*, 2018, **14**, 6303–6312.
139 R. J. Macfarlane, B. Lee, M. R. Jones, N. Harris, G. C. Schatz and C. A. Mirkin, *Science*, 2011, **334**, 204–208.
140 T. I. N. G. Li, R. Sknepnek, R. J. MacFarlane, C. A. Mirkin and M. Olvera De La Cruz, *Nano Lett.*, 2012, **12**, 2509–2514.
141 S. Wang, S. Lee, J. S. Du, B. E. Partridge, H. F. Cheng, W. Zhou, V. P. Dravid, B. Lee, S. C. Glotzer and C. A. Mirkin, *Nat. Mater.*, 2022, **21**, 580–587.
142 T. Vo, *AIChE J.*, 2023, e18243.
143 X. Chen, T. Vo and P. Clancy, *Soft Matter*, 2023, **19**, 8625–8634.
144 K. C. Elbert, W. Zygmunt, T. Vo, C. M. Vara, D. J. Rosen, N. M. Krook, S. C. Glotzer and C. B. Murray, *Sci. Adv.*, 2021, **7**, eabf9402.

145 Y. Zhang, G. Giunta, H. Liang and M. Dijkstra, *J. Chem. Phys.*, 2023, **158**, 184902.
146 M. N. O'Brien, M. R. Jones, B. Lee and C. A. Mirkin, *Nat. Mater.*, 2015, **14**, 833–839.
147 B. Luo, Z. Wang, T. Curk, G. Watson, C. Liu, A. Kim, Z. Ou, E. Luijten and Q. Chen, *Nat. Nanotechnol.*, 2023, **18**, 589–595.
148 E. Galati, H. Tao, M. Tebbe, R. Ansari, M. Rubinstein, E. B. Zhulina and E. Kumacheva, *Angew. Chem., Int. Ed.*, 2019, **58**, 3123–3127.
149 R. M. Choueiri, E. Galati, H. Thérien-Aubin, A. Klinkova, E. M. Larin, A. Querejeta-Fernández, L. Han, H. L. Xin, O. Gang, E. B. Zhulina, M. Rubinstein and E. Kumacheva, *Nature*, 2016, **538**, 79–83.
150 N. Kern and D. Frenkel, *J. Chem. Phys.*, 2003, **118**, 9882–9889.
151 A. Kim, K. Akkunuri, C. Qian, L. Yao, K. Sun, Z. Chen, T. Vo and Q. Chen, *ACS Nano*, 2023, **18**, 950.
152 A. Neophytou, V. N. Manoharan and D. Chakrabarti, *ACS Nano*, 2021, **15**, 2668–2678.
153 R. Guo, J. Mao, X. M. Xie and L. T. Yan, *Sci. Rep.*, 2014, **4**, 1–7.
154 X. Sen Hou, G. L. Zhu, L. J. Ren, Z. H. Huang, R. Bin Zhang, G. Ungar, L. T. Yan and W. Wang, *J. Am. Chem. Soc.*, 2018, **140**, 1805–1811.
155 E. Bianchi, J. Largo, P. Tartaglia, E. Zaccarelli and F. Sciortino, *Phys. Rev. Lett.*, 2006, **97**, 168301.
156 D. F. Tracey, E. G. Noya and J. P. K. Doye, *J. Chem. Phys.*, 2019, **151**, 224506.
157 D. F. Tracey, E. G. Noya and J. P. K. Doye, *J. Chem. Phys.*, 2021, **154**, 194505.
158 N. Pakalidou, J. Mu, A. J. Masters and C. Avendanõ, *Mol. Syst. Des. Eng.*, 2020, **5**, 376–384.
159 D. S. Sholl and R. P. Lively, *Nature*, 2016, **532**, 435–437.
160 X. Qian, M. Ostwal, A. Asatekin, G. M. Geise, Z. P. Smith, W. A. Phillip, R. P. Lively and J. R. McCutcheon, *J. Membr. Sci.*, 2022, **645**, 120041.
161 M. D. Eldridge, P. A. Madden and D. Frenkel, *Nature*, 1993, **365**, 35–37.
162 N. Hunt, R. Jardine and P. Bartlett, *Phys. Rev. E*, 2000, **62**, 900.
163 A. Travesset, *Proc. Natl. Acad. Sci. U. S. A.*, 2015, **112**, 9563–9567.
164 A. V. Tkachenko, *Proc. Natl. Acad. Sci. U. S. A.*, 2016, **113**, 10269–10274.
165 T. Vo and S. C. Glotzer, *Proc. Natl. Acad. Sci. U. S. A.*, 2022, **119**, e2116414119.
166 M. S. Wertheim, *J. Stat. Phys.*, 1984, **35**, 19–34.
167 M. S. Wertheim, *J. Stat. Phys.*, 1984, **35**, 35–47.
168 M. S. Wertheim, *J. Stat. Phys.*, 1986, **42**, 459–476.
169 M. S. Wertheim, *J. Stat. Phys.*, 1986, **42**, 477–492.
170 M. S. Wertheim, *J. Chem. Phys.*, 1987, **87**, 7323–7331.
171 A. Haghmoradi, L. Wang and W. G. Chapman, *J. Phys.: Condens. Matter*, 2016, **28**, 244009.
172 F. Smallenburg, L. Filion and F. Sciortino, *J. Phys. Chem. B*, 2015, **119**, 9076–9083.
173 A. Haghmoradi, B. D. Marshall and W. G. Chapman, *J. Chem. Eng. Data*, 2020, **65**, 5743–5752.
174 L. Rovigatti, J. M. Tavares and F. Sciortino, *Phys. Rev. Lett.*, 2013, **111**, 168302.
175 M. Formanek, L. Rovigatti, E. Zaccarelli, F. Sciortino and A. J. Moreno, *Macromolecules*, 2021, **54**, 6613–6627.
176 B. D. Marshall and W. G. Chapman, *Soft Matter*, 2014, **10**, 5168–5176.
177 Y. Tian, J. R. Lhermitte, L. Bai, T. Vo, H. L. Xin, H. Li, R. Li, M. Fukuto, K. G. Yager, J. S. Kahn, Y. Xiong, B. Minevich, S. K. Kumar and O. Gang, *Nat. Mater.*, 2020, **19**, 789–796.
178 T. Vo, V. Venkatasubramanian, S. Kumar, B. Srinivasan, S. Pal, Y. Zhang and O. Gang, *Proc. Natl. Acad. Sci. U. S. A.*, 2015, **112**, 4982–4987.
179 L. Tang, T. Vo, X. Fan, D. Vecchio, T. Ma, J. Lu, H. Hou, S. C. Glotzer and N. A. Kotov, *J. Am. Chem. Soc.*, 2021, **143**, 19655–19667.
180 P. Kumar, T. Vo, M. Cha, A. Visheratina, J. Y. Kim, W. Xu, J. Schwartz, A. Simon, D. Katz, V. P. Nicu, E. Marino, W. J. Choi, M. Veksler, S. Chen, C. Murray, R. Hovden, S. Glotzer and N. A. Kotov, *Nature*, 2023, **615**, 418–424.
181 G. Chen, K. J. Gibson, D. Liu, H. C. Rees, J. H. Lee, W. Xia, R. Lin, H. L. Xin, O. Gang and Y. Weizmann, *Nat. Mater.*, 2018, **18**, 169–174.
182 J. Choi, C. M. Hui, M. Schmitt, J. Pietrasik, S. Margel, K. Matyjazsewski and M. R. Bockstaller, *Langmuir*, 2013, **29**, 6452–6459.
183 Y. Wang, L. Dai, Z. Ding, M. Ji, J. Liu, H. Xing, X. Liu, Y. Ke, C. Fan, P. Wang and Y. Tian, *Nat. Commun.*, 2021, **12**, 1–8.
184 J. Zhou, M. N. Creyer, A. Chen, W. Yim, R. P. M. Lafleur, T. He, Z. Lin, M. Xu, P. Abbasi, J. Wu, T. A. Pascal, F. Caruso and J. V. Jokerst, *J. Am. Chem. Soc.*, 2021, **143**, 12138–12144.
185 N. Horst and A. Travesset, *J. Chem. Phys.*, 2016, **144**, 14502.
186 P. F. Damasceno, M. Engel and S. C. Glotzer, *ACS Nano*, 2012, **6**, 609–614.
187 F. Lu, K. G. Yager, Y. Zhang, H. Xin and O. Gang, *Nat. Commun.*, 2015, **6**, 1–10.
188 D. Morphew, J. Shaw, C. Avins and D. Chakrabarti, *ACS Nano*, 2018, **12**, 2355–2364.
189 J. Bohlin, A. J. Turberfield, A. A. Louis and P. Šulc, *ACS Nano*, 2023, **17**, 5387–5398.

